AD A121331

(5)

PROPELLANT CRACK TIP IGNITION AND PROPAGATION
UNDER RAPID PRESSURIZATION

SUMMARY REPORT

Prepared by
K. K. Kuo, M. Kumar, J. E. Wills,
J. G. Siefert, A. K. Kulkarni, E. Andiroglu,
S. T. Yu and J. P. Gore

October 1982

DTIC
ELECTE
NOV 10 1982

B

THE PENNSYLVANIA STATE UNIVERSITY
College of Engineering
Department of Mechanical Engineering
University Park, Pennsylvania

82 11 10 033

REPORT DOCUMENTATION PAGE		READ INSTRUCTIONS BEFORE COMPLETING FORM
1. REPORT NUMBER	2. GOVT ACCESSION NO. AD- P121351	3. RECIPIENT'S CATALOG NUMBER
4. TITLE (and Subtitle) PROPELLANT CRACK TIP IGNITION AND PROPAGATION UNDER RAPID PRESSURIZATION		5. TYPE OF REPORT & PERIOD COVERED Summary Sept. 1, 1981-Aug. 31, 1982
		6. PERFORMING ORG. REPORT NUMBER
7. AUTHOR(s) K. K. Kuo, M. Kumar, J. E. Wills, J. G. Siefert, A. K. Kulkarni, E. Andiroglu, S. T. Yu and J. P. Gore		8. CONTRACT OR GRANT NUMBER(s) N00014-79-C-0762
9. PERFORMING ORGANIZATION NAME AND ADDRESS Department of Mechanical Engineering The Pennsylvania State University University Park, PA 16802		10. PROGRAM ELEMENT, PROJECT, TASK AREA & WORK UNIT NUMBERS
11. CONTROLLING OFFICE NAME AND ADDRESS Office of Naval Research Power Program Arlington, Va. 22217		12. REPORT DATE October 1982
		13. NUMBER OF PAGES
14. MONITORING AGENCY NAME & ADDRESS(if different from Controlling Office)		15. SECURITY CLASS. (of this report) Unclassified
		15a. DECLASSIFICATION/DOWNGRADING SCHEDULE

16. DISTRIBUTION STATEMENT (of this Report)

Approved for public release; distribution unlimited

17. DISTRIBUTION STATEMENT (of the abstract entered in Block 20, if different from Report)

18. SUPPLEMENTARY NOTES

19. KEY WORDS (Continue on reverse side if necessary and identify by block number)

Ignition, Deflagration-to-Detonation Transition, Crack Propagation, AP-Composite Propellant, Ignition Delay, Stagnation Point Heat Transfer, Microstructure Damage, Crack Branching, Finite Element Stress Analysis

20. ABSTRACT (Continue on reverse side if necessary and identify by block number)

(see next page)

DD FORM 1 JAN 73 1473   EDITION OF 1 NOV 65 IS OBSOLETE

ABSTRACT

Two major tasks performed during the report period were investigation of: (i) crack tip ignition phenomena under rapid pressurization and (ii) crack propagation in burning solid propellants.

Ignition of AP-based composite solid propellants located at the tip of an inert crack was investigated both experimentally and theoretically. The ignition process was observed by simultaneously using a high-speed (~40,000 pictures/s) camera and a fast-response photodiode system. Heat flux to the propellant surface was measured with a thin-film heat-flux gage. Effects of pressurization rate, crack-gap width, and igniter flame temperature on the ignition process were studied experimentally. Results indicate that the ignition-delay time decreases and the heat flux to the propellant surface increases as the pressurization rate is increased. The decrease in ignition delay with increasing pressurization rate is caused by enhanced heat feedback to the propellant surface at higher pressurization rates. This augmentation in heat feedback to the propellant at higher pressurization is believed to be a result of a combination of the following mechanisms: heating due to compression-wave reflection at the closed end; heat release due to burning of unreacted igniter species (or particles) near the tip, behind the compression wave; and enhanced heat transfer due to recirculating hot gases near the tip.

In the theoretical investigation of the tip ignition event a comprehensive model for ignition of AP-based composite solid propellants was developed and numerical solutions were obtained. The analysis simulates the ignition process of a propellant sample, located in a stagnation region, under rapid pressure loading conditions. Specific features considered in the model include: a) detailed chemical kinetics information for the ignition of AP-based composite propellants; b) two-dimensional (axisymmetric) geometry for the composite propellant; and c) rapid pressurization of the gas phase. An implicit finite difference scheme was used to solve the set of transient, second-order, coupled, inhomogeneous, nonlinear, governing partial differential equations. Numerical solutions revealed a number of important events occurring during the ignition sequence. These include: igniter gas penetration to the region near the sample surface; combustion of unburned species upon arrival of compression waves; heat transfer to the propellant; pyrolysis of oxidizer and fuel; and gas-phase reactions leading to ignition. The model predicts the experimental observation that the ignition delay time decreases as the pressurization rate is increased. Various ignition criteria considered showed the same trend as experimentally measured.

Crack propagation in a burning composite solid propellant subjected to rapid pressurization in the order of 10 GPa/s was investigated experimentally. A visual record of the event was made using a high-speed movie camera. The transient pressurization process was recorded by high-frequency pressure transducers in the combustion chamber. The effect of pressurization rate on both crack propagation velocity and time variation of crack shape was studied. Experimental results indicated that the crack velocity increases as the pressurization rate is raised. The measured dependence of crack propagation velocity on pressurization rate was found to be stronger than that based only upon viscoelastic material property variation at different loading rates. A characteristic difference of crack geometry variation during propagation was observed at different pressurization rates. At higher pressurization rates, the geometric transformation of the crack tip was

ABSTRACT

(Continued)

preceded by emergence of a fan region immediately above the crack tip. It is
believed that the fan region is created by micro-structure damage in the propel-
lant at the crack tip, which allows the bright combustion gases to spread ahead
of the tip region in a radial fashion. The actual geometric change, a trans-
formation of the crack shape from a smooth triangular contour into a square
contour with a jagged leading edge, is believed to be the growth of small frac-
tures into major crack branches.

PROPELLANT CRACK TIP IGNITION AND PROPAGATION
UNDER RAPID PRESSURIZATION

SUMMARY REPORT

Sponsored by

Prepared by

Kenneth K. Kuo, Telephone (814) 865-6741
Mridul Kumar, Telephone (412) 665-6638
John E. Wills, Telephone (814) 863-2699
John G. Siefert, Telephone (814) 863-2699
Anil K. Kulkarni, Telephone (814) 865-7073
Esber Andiroglu, Telephone (814) 863-2699
S. T. Yu, Telephone (814) 863-2699
Jayavant P. Gore, Telephone (814) 863-1506

Department of Mechanical Engineering
The Pennsylvania State University
University Park, PA 16802

ACKNOWLEDGEMENTS

TABLE OF CONTENTS

LIST OF FIGURES

LIST OF TABLES

Nomenclature

c, c_p	specific heat
D	binary mass diffusion coefficient
E	activation energy
G	external radiation heat flux
I_z	local radiation flux at z
k	thermal conductivity
k_i	rate constants for reaction i
L	thickness of oxidizer pellet
m	constant defined in Eq. (31)
P	pressure
$\dot{q}''$	heat flux (energy per unit time per unit area)
$\dot{q}'''$	heat generation rate (energy per unit time per unit volume)
Q_{py}	heat of pyrolysis per unit mass
r	radial distance from center of statistically averaged element
r_b	burning rate
R	gas constant
R_u	universal gas constant
R_1, R_2	radii of outer surfaces of oxidizer particle and fuel binder, respectively .
t	time
T	temperature
v_z	gas phase velocity in z direction
$\overline{W}$	average molecular weight
Y_j	mass fraction of species j in gas phase
z	distance from initial (t=0) position of interface; positive in gas phase
Z	pre-exponential factor
α	radiation absorptivity of interface

β	in-depth radiation absorption coefficient
ρ	density
τ	transmissivity of solid phase
$\dot{\omega}''$	mass production rate per unit area
$\dot{\omega}_i'''$	mass production rate per unit volume

Subscripts

1,2,3,4,5	various reactions or species
F	fuel
F-g	fuel-gas interface
g	gas-phase
i	initial value or species i
Ox	oxidizer
Ox-F	oxidizer-fuel interface
Ox-g	oxidizer-gas interface
py	pyrolysis
s	solid phase
s-g	solid-gas interface
z	z in z direction

I. INTRODUCTION

This report summarizes progress made during the period September 1, 1981 to August 31, 1982, under the project entitled "Ignition of Solid Propellants and Propagation of Burning Propellant Cracks" (Contract No. N00014-79-C-0762).

The overall objective of this investigation is to achieve better understanding of the ignition mechanism under transient pressure loading conditions and to investigate propagation of burning solid propellant cracks. These fundamental studies are expected to help in providing insight into convective burning and evolution of deflagration-to-detonation transition (DDT) processes in damaged solid propellant grains. Specific objectives of this study are:

1. To numerically solve the theoretical model[1] for ignition of AP-based composite solid propellants under rapid pressure loading conditions.

2. To study the effect of such parameters as pressurization rate and oxidizer particle size on the ignition process.

3. To validate the theoretical model by comparing predicted results with experimental data.

4. To examine the effect of various ignition criteria on predicted results.

5. To observe crack propagation process in burning solid-propellant samples under rapid gas loading conditions.

6. To measure crack propagation velocities in burning propellant samples.

7. To study the effect of pressurization rate on crack propagation velocity.

The following is a list of papers[12-19] published during the past year under the support of this contract.

1. "Ignition of Composite Propellants in a Stagnation Region Under Rapid Pressure Loading," Nineteenth International Symposium on Combustion, Haifa, Israel, August 1982, by M. Kumar, J. E. Wills, A. K. Kulkarni, and K. K. Kuo.

2. "A Comprehensive Ignition Model for Composite Solid Propellants," Eighteenth JANNAF Combustion Meeting, Pasadena, California, CPIA Publication 347, Vol. III, October 1981, pp. 215-224 by A. K. Kulkarni, M. Kumar, and K. K. Kuo.

3. "Investigation of Composite Propellant Ignition Under Rapid Pressurization," Eighteenth JANNAF Combustion Meeting, Pasadena, California, CPIA Publication 347, Vol. III, October 1981, pp. 243-262 by J. E. Wills, M. Kumar, A. K. Kulkarni, M. Hund, and K. K. Kuo.

4. "Abrupt Ignition of AP-Based Composite Propellants Under Severe Gas Loading Conditions," 1982 JANNAF Propulsion Systems Hazards Meeting, China Lake, California, April 1982, by J. E. Wills, M. Kumar, A. K. Kulkarni, and K. K. Kuo.

5. "A Model for AP-Based Composite Propellant Ignition, Including Gas-Phase and Subsurface Reactions," AIAA Paper No. 82-1109, AIAA/ASME/SAE Joint Propulsion Conference, Cleveland, Ohio, June 1982, by M. Kumar, J. E. Wills, A. K. Kulkarni, and K. K. Kuo.

6. "Experimental Observations of Crack Propagation in Burning Solid Propellants," Nineteenth JANNAF Combustion Meeting, Greenbelt, Maryland, October 1982, by J. G. Siefert and K. K. Kuo.

7. "Effect of Deformation on Flame Spreading and Combustion in Propellant Cracks," AIAA Journal, Vol. 19, Dec. 1981, pp. 1580-1589 by M. Kumar and K. K. Kuo.

8. "A Review of Solid Propellant Ignition Studies," AIAA Journal, Vol. 20, Feb. 1982 by A. K. Kulkarni, M. Kumar, and K. K. Kuo

II. INVESTIGATION OF COMPOSITE PROPELLANT IGNITION

2.1 Brief Description of Ignition Model

The modified mathematical model is presented briefly below. More details of the model can be found in our last annual report.[1] The model simulates ignition of a composite propellant in a stagnation region. The physical model considers a cylindrical oxidizer particle having radius R_1 and length L embedded in a cylindrical binder of radius R_2 in such a way that initially the oxidizer and fuel binder surfaces are in the same plane (see Figs. 1 and 2). For the coordinates shown in Fig. 2, the solid-phase equations are

$$\text{Oxidizer:} \quad \rho_{Ox,s} c_{Ox,s} \frac{\partial T}{\partial t} = \frac{\partial}{\partial z}\left(k_{Ox,s} \frac{\partial T}{\partial z}\right) + \frac{1}{r}\frac{\partial}{\partial r}\left(k_{Ox,s} r \frac{\partial T}{\partial r}\right) + \dot{q}'''_{Ox,s} \tag{1}$$

$$\text{Fuel:} \quad \rho_{F,s} c_{F,s} \frac{\partial T}{\partial t} = \frac{\partial}{\partial z}\left(k_{F,s} \frac{\partial T}{\partial z}\right) + \frac{1}{r}\frac{\partial}{\partial r}\left(k_{F,s} r \frac{\partial T}{\partial r}\right) + \dot{q}'''_{F,s} \tag{2}$$

CROSS-SECTIONAL VIEW   TOP VIEW

OXIDIZER
PARTICLE

FUEL BINDER
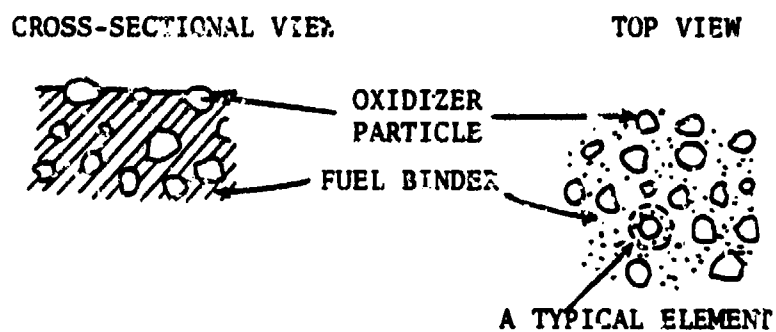
A TYPICAL ELEMENT

Fig. 1   Typical Composite Propellant Structure

IGNITER GAS

GAS PHASE

z (I)

r (J)

L

OXIDIZER

R_1

R_2

FUEL BINDER

ADIABATIC
BOUNDARIES
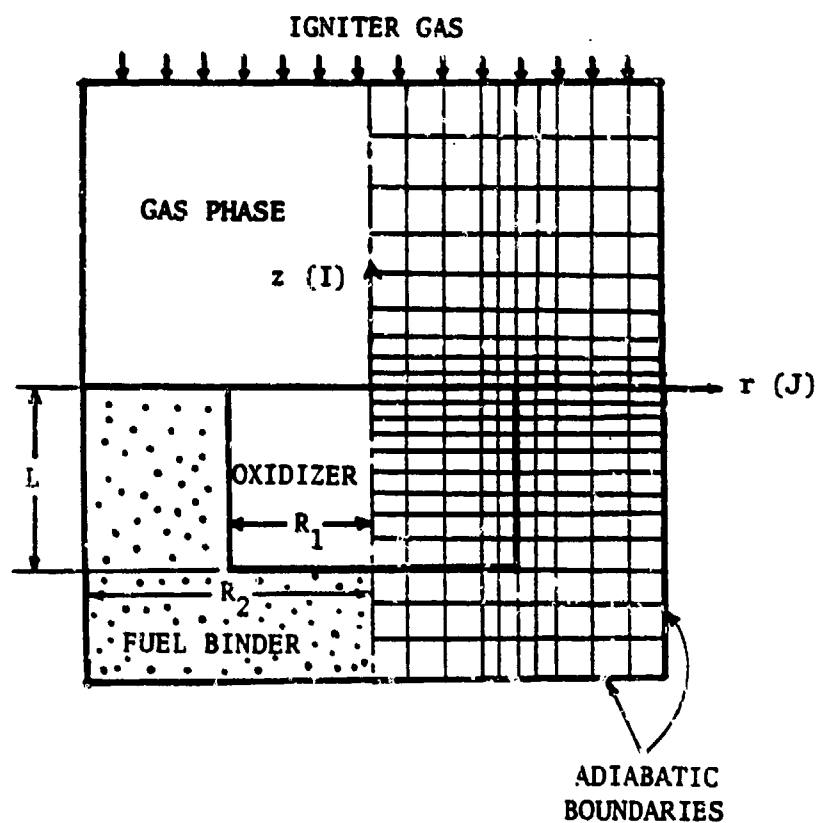
Fig. 2   Cross-Sectional View of a Statistically
Averaged Element and Finite Difference
Grid Pattern

where

$$\dot{q}'''_{Ox,s} = \dot{q}'''_{Ox, \text{radiation}} + \dot{q}'''_{Ox,\text{pyrolysis}} \tag{3}$$

$$\dot{q}'''_{Ox,\text{radiation}} = \tau_{Ox} G \beta_{Ox} e^{-\beta_{Ox} z} = \beta_{Ox} I_z \tag{4}$$

and

$$\dot{q}'''_{Ox,\text{pyrolysis}} = - Z_{Ox,py} Q_{Ox,py} \exp(-E_{Ox,py}/R_u T) \tag{5}$$

The expression for $\dot{q}'''_{F,s}$ is similar to that of $\dot{q}'''_{Ox,s}$.

The gas-phase conservation equations are

Continuity Eq:
$$\frac{\partial \rho_g}{\partial t} + \frac{\partial (\rho_g v_z)}{\partial z} = 0 \tag{6}$$

Energy Eq:
$$c_p \rho_g \frac{\partial T}{\partial t} + \rho_g c_p v_z \frac{\partial T}{\partial z} - \frac{\partial P}{\partial t} = \frac{\partial}{\partial z} \left(k_g \frac{\partial T}{\partial z} \right)$$

$$+ \frac{1}{r} \frac{\partial}{\partial r} \left(k_g r \frac{\partial T}{\partial r} \right) + \dot{q}'''_g \tag{7}$$

Species Eq:
$$\rho_g \frac{\partial Y_j}{\partial t} + \rho_g v_z \frac{\partial Y_j}{\partial z} = \frac{\partial}{\partial z} \left(\rho_g D \frac{\partial Y_j}{\partial z} \right)$$

$$+ \frac{1}{r} \frac{\partial}{\partial r} \left(\rho_g D r \frac{\partial Y_j}{\partial r} \right) + \dot{\omega}'''_j \tag{8}$$

where $j = 1$, 2, 3 and 4 for the gas phase species, oxidizer, NH_3, $HClO_4$, and fuel, respectively.

The gas-phase momentum equations are replaced by the measured

$$P = P(t) \tag{9}$$

The equation of state for the gas phase is

$$\rho_g = \frac{P \bar{W}}{R_u T} \tag{10}$$

The following basic assumptions are employed in the mathematical model:

1) The solid propellant and gas phase are two-dimensional axisymmetric.

2) The gas-phase pressure is a prescribed function of time, and is uniform in a small region adjacent to the solid propellant.

3) Gases obey the perfect gas law.

4) Chemical reactions and pyrolysis processes can be described by Arrhenius expressions.

5) Binary diffusion coefficients of all species are equal.

6) Prior to ignition, displacement of the propellant surface due to regression can be neglected.

7) The radial bulk velocity is much smaller than the axial.

The initial and boundary conditions for the solid phase (both fuel and oxidizer) are

$$\text{at } t = 0 \quad : \quad T(0,r,z) = T_i \tag{11}$$

$$\text{at } z \to -\infty \quad : \quad T = T_i \tag{12}$$

$$T\big|_{r=R_1^+} = T\big|_{r=R_1^-} \quad \text{and} \quad T\big|_{z=-L^-} = T\big|_{z=-L^+} \tag{13}$$

$$\text{on } r = 0 \quad : \quad \frac{\partial T}{\partial r} = 0 \tag{14}$$

$$\text{and on } r = R_2 \quad : \quad \frac{\partial T}{\partial r} = 0 \tag{15}$$

$$\text{at } z = z_{s-g} \quad : \quad k_s \frac{\partial T}{\partial z}\bigg|_{z_{s-g}^-} = k_g \frac{\partial T}{\partial z}\bigg|_{z_{s-g}^+} + \alpha_{s-g} G + \tag{16}$$

$$r_{b_s} \rho_s T(c_{P_s} - c_{pg}) + q''_{s-g}$$

$$\text{at } z = -L \quad : \quad k_{F,s} \frac{\partial T}{\partial z}\bigg|_{-L} = k_{Ox,s} \frac{\partial T}{\partial z}\bigg|_{-L^+} + \tag{17}$$

$$\alpha_{Ox-F} \tau_{Ox} G e^{-\beta_{Ox} L}$$

at $r = R_1$ and $-L < z < 0$: $\quad -k_{F,s}\left.\dfrac{\partial T}{\partial r}\right|_{R_1^+} =$

$$-k_{Ox,s}\left.\dfrac{\partial T}{\partial r}\right|_{R_1^-} \tag{18}$$

Initial and boundary conditions for the gas-phase equations (for $j = 1, 2, 3, 4$) are

at $t = 0$: $\quad v_z(0,r,z) = 0$; $\quad T(0,r,z) = T_{g,i}$;

$$Y_j(0,r,z) = Y_{j,i} \tag{19}$$

on $r = 0$: $\quad \dfrac{\partial T}{\partial r} = 0$; $\dfrac{\partial Y_j}{\partial r} = 0$ $\tag{20}$

and on $r = R_2$: $\quad \dfrac{\partial T}{\partial r} = 0$; $\dfrac{\partial Y_j}{\partial r} = 0$ $\tag{21}$

$z \to \infty$: $\quad \dfrac{\partial T}{\partial z} = 0$; $\dfrac{\partial Y_j}{\partial z} = 0$ $\tag{22}$

on $z = z_{s-g}$: $\quad T\big|_{z_{s-g}^+} = T\big|_{z_{s-g}^-}$ $\tag{23}$

on $z = z_{s-g}$: $\quad \rho_g v_z = \rho_s r_{b_s}$ $\tag{24}$

and $\rho_g v_z Y_j\big|_{z_{s-g}^-} = \rho_g v_z Y_j\big|_{z_{s-g}^+} - \rho_g D \dfrac{\partial Y_j}{\partial z} - \dot{\omega}_j''$ $\tag{25}$

The following reactions are considered in the model.[2-7]

$$AP_{(s)} \xrightarrow[\substack{\text{Exothermic}\\\text{Degradation}}]{k_1} Ox_{(g)} \tag{26}$$

$$AP_{(s)} \xrightarrow[\substack{\text{Dissociative}\\\text{Sublimation}}]{k_2} NH_{3(g)} + NClO_{4(g)} \tag{27}$$

$$NH_{3(g)} + HClO_{4(g)} \xrightarrow[\substack{Premixed \\ A/PA\ Reaction}]{k_3} Ox_{(g)} \tag{28}$$

$$PBAA_{(s)} \xrightarrow[Pyrolysis]{k_4} Fuel_{(g)} \tag{29}$$

$$Ox_{(g)} + Fuel_{(g)} \xrightarrow[\substack{Diffusion \\ Flame}]{k_5} Products_{(g)} \tag{30}$$
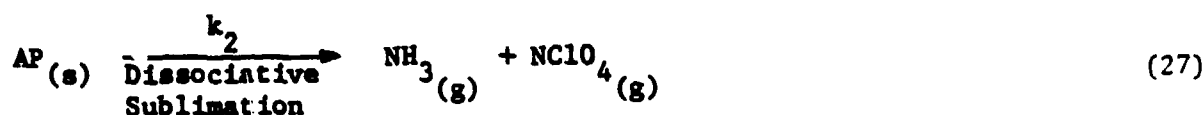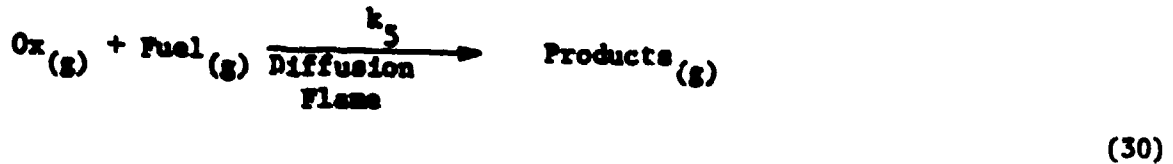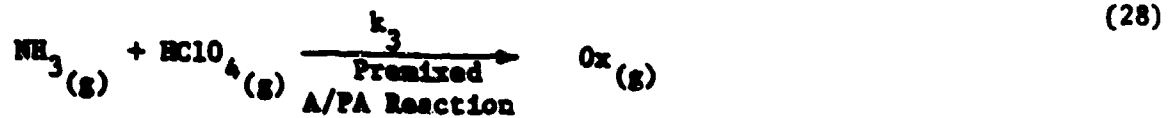
The reaction rate constant is approximated by

$$k = Z\ T^m e^{-E/R_u T} \tag{31}$$

If the gas-phase mass fractions, Y_1, Y_2, Y_3, Y_4, Y_5, represent the oxidizer, ammonia, perchloric acid, fuel, and products, respectively, the source terms can be expressed as follows.

$$\dot{\omega}_1''' = Z_3 \frac{W_1}{W_2 W_3} \rho_g^2 Y_2 Y_3\ T\ \exp\ (-E_3/R_u T) \tag{32}$$

$$-Z_5 \frac{1}{W_4} \rho_g^2 Y_1 Y_4\ \exp\ (-E_5/R_u T) \tag{33}$$

$$\dot{\omega}_2''' = Z_3 \frac{1}{W_3} \rho_g^2 Y_2 Y_3\ T\ \exp\ (-E_3/R_u T) \tag{33}$$

$$\dot{\omega}_3''' = \dot{\omega}_2''' \frac{W_3}{W_2} \tag{34}$$

$$\dot{\omega}_4''' = -Z_5 \frac{1}{W_1} \rho_g^2 Y_1 Y_4\ \exp\ (-E_5/R_u T) \tag{35}$$

$$\dot{q}_g''' = (\dot{\omega}_2''' \Delta H_3 + \dot{\omega}_4''' \Delta H_5) \tag{36}$$

The following paragraphs list differences in the model presented above from that given in Ref. 1. (Complete solution of the ignition model for composite propellants is presented in Section 2.3.)

1. In our previous version, axial diffusion of species in the gas phase was neglected; it has been reinstated in the current model. This was done because it was found that very near the propellant surface the axial species concentration gradients can be extremely steep which are comparable to the axial convection or radial diffusion.

2. In the solid-phase energy equation, the inhomogeneous terms $\dot{q}'''_{Ox,s}$ and $\dot{q}'''_{F,s}$ included heat generation due to photochemical reactions. To model this term, values of Q_{pc_λ} (rate of heat generation due to photochemical process per unit wavelength of radiation) and η_λ (efficiency for photochemical process at wavelength λ) are needed for both the fuel and oxidizer. These are not available in the literature, and also the contribution by the photochemical reaction was thought to be small in AP/PBAA propellant. Therefore, this term is neglected in the current model.

3. The total energy loss by radiation from the propellant surface to the environment, $\epsilon_s E_{bs}$, (which appears in the energy balance at the solid-gas interface was estimated to be small compared to convective and conductive heat transfer during the ignition process, therefore it has been neglected.

4. Heat release due to reactions at the solid-gas interface, $\dot{q}''_{s-g}$, was restricted to latent heat of gasification represented by $r_{b_s} \rho_s [\Delta h_{f,s} - \Delta h_{f,g}]$. No heterogeneous chemical reactions were considered due to the lack of adequate information on heterogeneous chemical reactions in AP/PBAA propellant ignition. Heat generation due to reactions at the fuel-oxidizer interface in the solid phase is also neglected because previous investigations did not find evidence of such reactions for AP composite propellants.

5. Far away from the propellant surface ($z \to \infty$), a new boundary condition had to be added because of the inclusion of axial diffusion term in the species equation. Therefore, $\frac{\partial Y_i}{\partial z} = 0$, was imposed to prevent any species diffusion at the far-field boundary. It should be noted, however, the species can still be transported across this boundary by convection.

6. Far away from the propellant surface ($z \to \infty$), $\frac{\partial T}{\partial z} = 0$; because the spatial variation in temperature is not expected to be present there.

7. There were some minor typographical errors in the model presented in the last annual report:[1] a) the term (1/T) in the expressions for $\dot{\omega}_1'''$ and $\dot{\omega}_2'''$ were replaced by T. b) The negative sign appearing in the equation for $\dot{q}_g'''$ should be positive. c) Some signs in the energy balance at the interface $z = -L$ have also been corrected.

2.2 Computer Program Development

A finite difference technique has been used to develop a computer program to solve the composite propellant ignition model. A set of nine coupled, nonlinear, inhomogeneous, partial differential equations along with a complete set of initial and boundary conditions make up the mathematical model. As a result of this complexity, no analytical solutions exist or could be developed; therefore, numerical solution was the only alternative to obtain theoretical predictions.

2.2.1 Special Features of the Numerical Scheme

Several common features described in the following were used to obtain an accurate solution. Because large temperature and species concentration gradients exist near the propellant surface, a coordinate transformation was performed on the z-axis to obtain an exponentially finer grid spacing in the real coordinate while maintaining a constant grid spacing in the transformed coordinate.

$$\text{Solid phase:} \quad s = \exp(A_s z) - 1 \quad \text{or,} \quad z = \frac{1}{A_s} \ln (1+s) \tag{37}$$

$$\text{Gas phase:} \quad s = 1 - \exp(-A_g z) \quad \text{or,} \quad z = -\frac{1}{A_g} \ln(1-s) \tag{38}$$

In order to control possible stability problems, a generalized Crank-Nicolson technique was employed to solve the system. Allen's method was utilized to approximate the radial derivatives with a variable grid size while a three point central difference scheme was used to approximate the axial derivatives with a constant grid spacing.

Quasilinearization of the inhomogeneous terms was required because the source terms in the governing equations are implicitly dependent upon temperature and species concentration. Finally, a successive overrelaxation iterative scheme was chosen to solve a larger set of algebraic, finite-difference equations.

Appendix A describes the details of the abovementioned numerical techniques.

2.2.2 Methods Used in Checking Numerical Solutions

There were three major checks made on the computer solution to ensure that numerical solutions obtained are the genuine solutions of the theoretical model:

i) Comparison with available analytical solution - to show that the numerical solutions for simplified geometric configuration under known surface heat flux agree with the classical analytical solutions.

ii) Global energy balance - to sum the net heat addition to all elemental volumes in the solid phase and to verify that the overall energy balance is achieved.

iii) Local energy balance check - to examine whether the numerical solution can satisfy the governing differential equations and boundary conditions.

All three independent checks verify that the numerical solution obtained from the computer code represents the correct solution of the partial differential equations in the theoretical model.

2.2.3 Current Status of the Computer Code

One year ago, the computer code was only capable of solving simplified cases in which measured heat flux to the propellant surface was used as an input to the solid-phase energy equations. Only the solid-phase portion of the whole physical model was implemented and fully debugged; the gas-phase portion was partly coded. Currently, the complete model including both gas- and solid-phase equations has been implemented, debugged, and tested. A layout of the flow diagram of the computer code is given in Fig. 3.

At the present time, the computer program is capable of predicting ignition process for AP/PBAA propellants only because the current reaction mechanism is specific to the above propellant. However, the program can be extended to solve for any other propellant as long as the reaction mechanism for that propellant is prescribed. In the near future, the ignition mechanism for nitramine propellants will be incorporated into the model and will subsequently be implemented in the computer code. Also, the computer code which is presently executing on IBM 370/3018 will be installed on PDP 11/23 to reduce the computer cost.

2.3 Numerical Solutions and Comparison with Experimental Results

2.3.1 Input Parameters and Initial Conditions

Numerical values of the important input parameters to the computer programs are listed in Table 1. Thermal properties of AP were taken from Ref. 8. Thermal properties of PBAA are approximate and are identical to those used by Varney and Strahle.[7] Thermal conductivity of PBAA was deduced from the average density of fuel and the value of thermal diffusivity used in Ref. 7 for fuel binders. Thermal properties for the gas phase were obtained by averaging the thermal properties of the combustion product species of the AP/PBAA propellant. The thermal conductivity is assumed to vary as $T^{0.75}$. The composition of these product species was determined from the NASA-Lewis chemical equilibrium calculation program.[10] Molecular weights of the gas-phase species were obtained in a similar fashion.
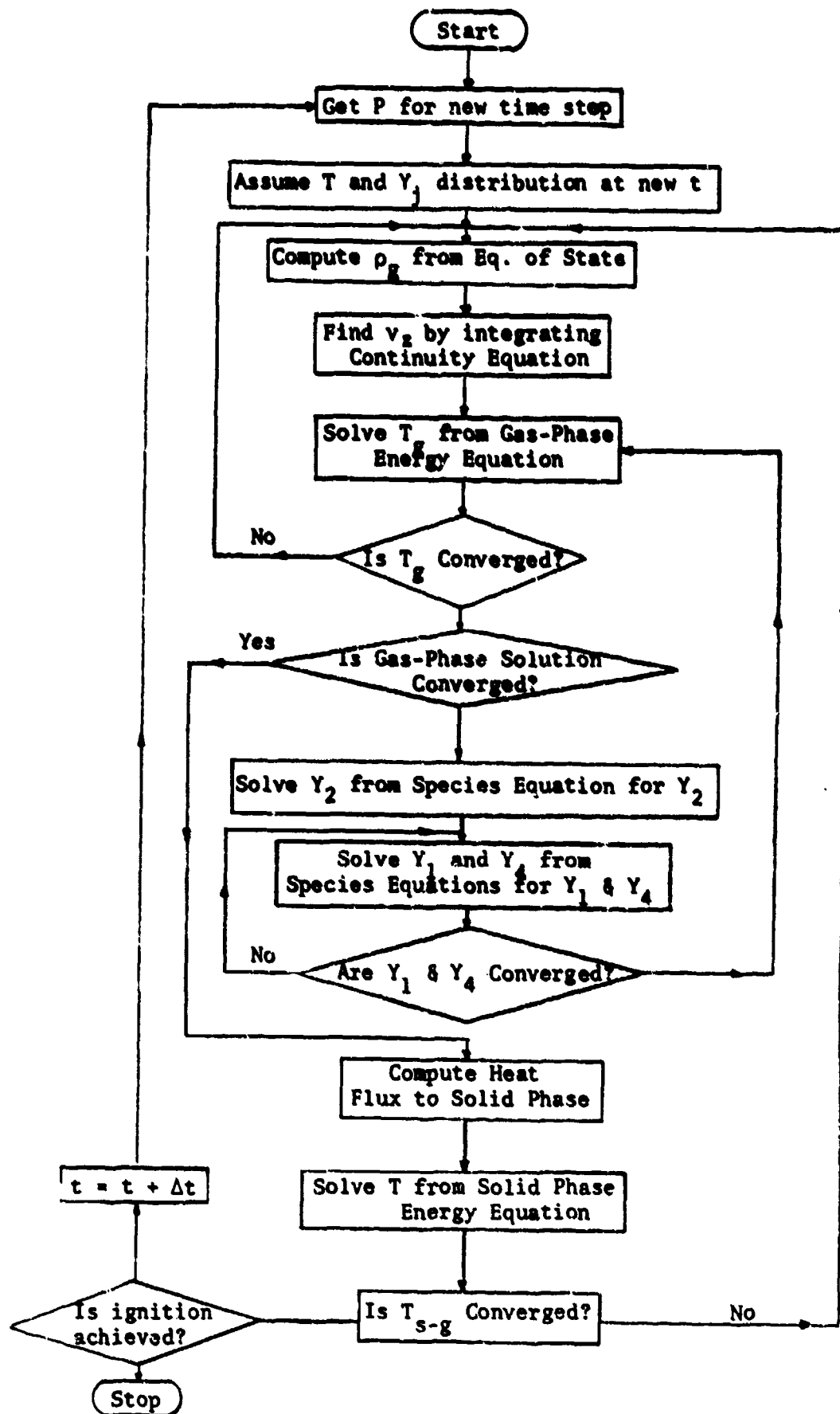
Fig. 3 General Layout of Computational Flow Diagram

Table 1 Physical Properties and Input Parameters

Property	Units	Gas Phase	Solid Phase	
			AP	PBAA
c	J/kg.K	1922	1305	1255
k	W/m.K	$0.228 \, (T/300)^{0.75}$	0.46	0.12
	m²/s	0.2×10^{-4}	---	---
L^a	μm	---	---	---
R_1^a	μm	---	30.6	---
R_2^a	μm	---	---	40
ρ	kg/m³	P/RT	1950	947
W	kg/kmol	$W_1 = 29.2, \; W_3 = 17.0,$	117.5	100.8
		$W_3 = 100.5, \; W_4 = 24.5.$		
		$W_5 = 20.4$		

^{a}For AP particle size of 76 μm and 75% solids loading

Table 2 Chemical Kinetic Constants

Reaction Number [see Eqs. (26)-(30)]	Activation Energy E (J/kmol)	Heat of Reaction ΔH(J/kg)	m (see Eq. 31)	Order of Reaction
1	1.00×10^8	-1.61×10^6	0	0
2	1.00×10^8	2.07×10^6	0	0
3	0.65×10^8	-2.23×10^7	1	2
4	1.13×10^8	2.38×10^5	0	0
5	0.42×10^8	-1.86×10^6	0	2

Numerical values of chemical kinetic constants are given in Table 2. Some of the activation energies given in Table 2 are approximate due to lack of kinetic data. It should be noted that chemical kinetics of ignition may differ significantly from those of steady-state combustion. It is generally believed that AP pyrolysis consists of 70% exothermic degradation and 30% dissociative sublimation.[2] The activation energy of this decomposition is estimated to be between 20-30 kcal/mole.[2-7] In the present study, the value was taken as 24 kcal/mole. The activation energy of the premixed reaction between NH_3 and $HClO_4$ is 15.5 kcal/mole.[3] The pyrolysis of fuel (PBAA) is endothermic. The activation energy for fuel pyrolysis was taken as 113 kJ/mole (27 kcal/mole); Ninan and Krishman[11] have shown that for many polybutadiene binders the activation energy for thermal decomposition is around 110 kJ/mole. (It may be noted that Varney and Strahle[9] reported the activation energy for PBAA decomposition as 34 kcal/mole). The pyrolysis products of fuel and oxidizer react in the gas phase to form the final products, however, no reliable estimate of kinetic parameters for this reaction is available.

The initial conditions for computations were consistent with those encountered in the experiments. Initial pressure and temperature were 0.1 MPa and 300 K, respectively. In order to simulate the bright reaction zone observed near the tip (see Refs. 1 and 2), a mixture of gaseous oxidizers and fuel species was assumed to be present at t = 0. Pressure-time traces, used as input to the computer program, were either experimentally measured or prescribed for a given pressurization condition.

2.3.2 Ignition Criteria

Since there is no universally accepted ignition criterion (IC), several ignition criteria were employed to test the predictive capability of the model. The onset of ignition is defined as the time (1) when the local maximum of volumetric gas-phase heat release reaches a critical value $(\dot{q}'''_{g,max} > c)$, (2) when the AP pyrolysis rate near the radial oxidizer-fuel interface reaches a critical

value, (3) when the axial gas velocity at $r = R_1$ and a distance away from the surface is zero (i.e., when the surface blowing is sufficiently large to overcome the incoming gas velocity induced by pressurization of the cavity), (4) when the rate of maximum volumetric gas-phase heat release reaches a critical value, or (5) when the rate of AP pyrolysis rate reaches a critical value.

2.3.3 Discussion of Predicted Results

The general sequence of events leading to ignition, as revealed by the numerical solution is as follows.

As pressurization of the crack cavity begins, temperature in the crack increases; and gases flow toward the crack tip at high velocities (see Fig. 4a). The rise in gas temperature produces a temperature gradient at the solid-gas interface, heat is transferred to the solid propellant, and heating of the solid propellant begins. At the same time, as the gas temperature rises, the initial unreacted oxidizer and fuel species (from the igniter system) react, further increasing the local gas temperature as well as the heat flux to the propellant (see Fig. 5). This results in a continuous increase in the propellant surface temperature during the initial period.

As time progresses, the initial unreacted species present in the gas phase are completely consumed, and the temperature of the propellant surface continues to rise. This causes slight attenuation in the heat flux to the propellant surface. The heat flux increases very rapidly during the initial period and then levels off. The axial temperature distribution at the oxidizer fuel interface $(r = R_1)$ at various times is shown in Fig. 6. As seen in Fig. 6, the thermal wave penetration into the solid increases with time. Temperatures far from the surface are quite uniform (not shown in the figure). The reversal of maximum temperatures with time at 20 µm into the gas phase is caused by a relaxation from the initial reactions and a decreasing pressurization rate with time.
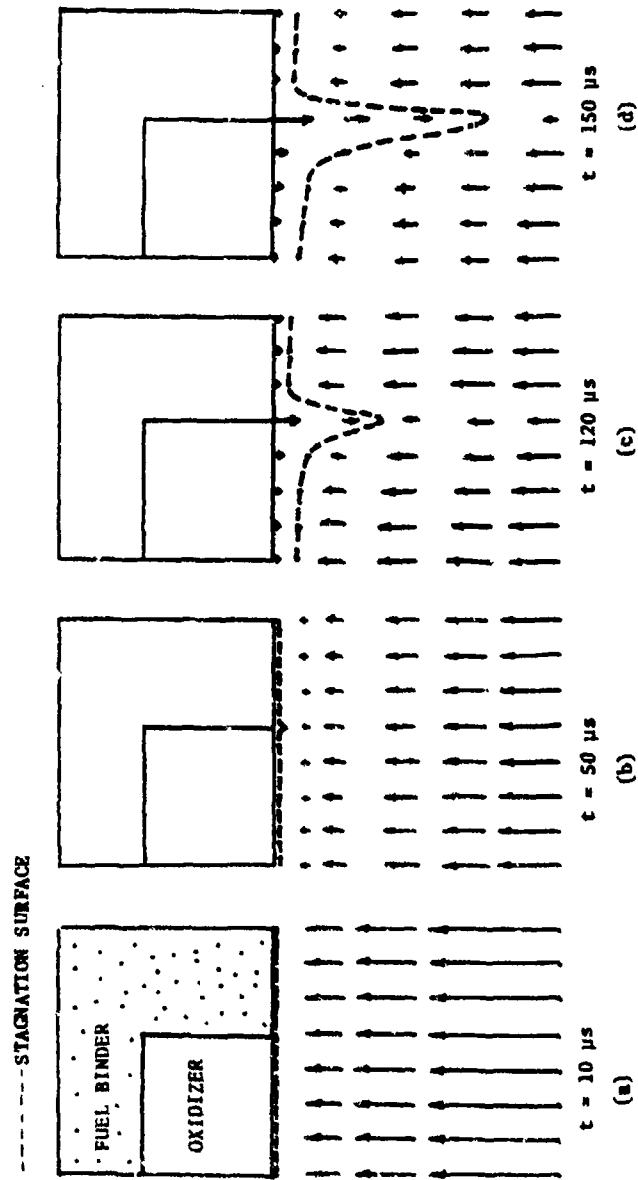
Fig. 4 Schematic of Sequential Variation of Axial Velocity
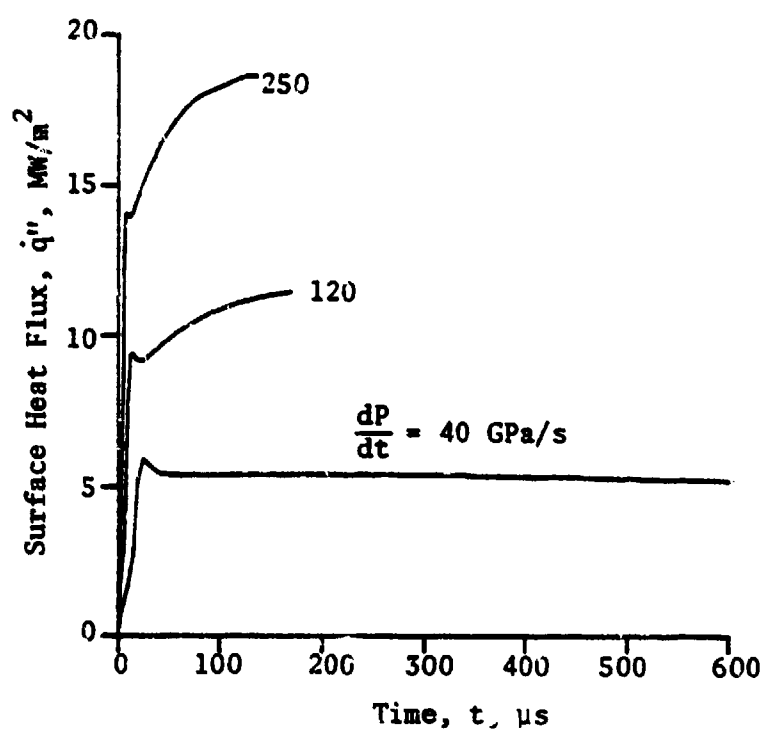Field Adjacent to Propellant Surface

Fig. 5 Calculated Time Variation of Surface
Heat Flux at AP/PBAA Interface ($r=R_1$)
for Various Pressurization Rates
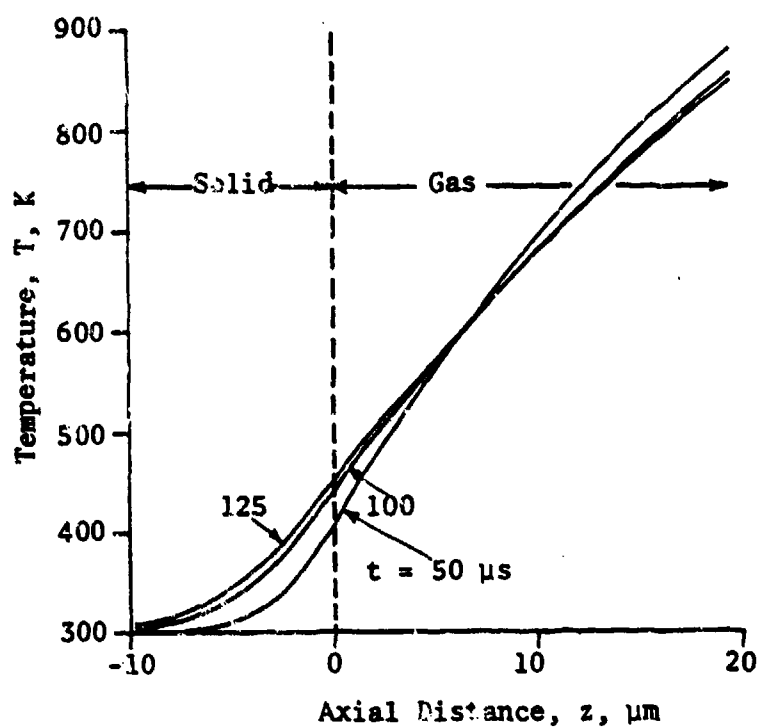
Fig. 6   Axial Temperature Variation at AP/PBAA Interface
(r=R$_1$) for Various Times (Average dP/dt = 120 GPA/s)

Since the thermal properties of AP and PBAA are very different, there is a steep and discontinuous temperature gradient near the AP/PBAA interface. Figure 7 shows the radial variation of propellant surface temperature as a function of time. Because PBAA has a lower thermal diffusivity and conductivity, its surface temperature rises much faster than that of AP. The gas-phase temperature near the propellant surface also changes with radius and is strongly coupled to the solid-gas interface temperature. Farther away from the propellant surface, the radial gas temperature variation diminishes. Contrary to the numerical results obtained here, which shows that the surface temperature of PBAA is much higher than the AP, Price et al.[11] deduced from studying AP/PBAA sandwiches in steady-state burning that the fuel surface temperature is lower than the AP. If the thermal diffusivity and conductivity of PBAA were larger than that of AP, Price's trend for surface temperature would be observed; however, the functional relationship of the predicted ignition delays versus pressurization rate, etc., will remain unchanged.

Figure 8 shows time variation of maximum volumetric gas-phase heat release. The gas-phase reaction between the unburned oxidizer and fuel species lasts for about 10 μs. During this interval the heat release rate is extremely high (the values are off the scale of Fig. 8). High initial concentration of the species causes the rate of heat generation to increase abruptly as the local temperature increases due to pressurization. The heat generation rate peaks and then drops to almost zero (even though the temperature continues to increase) since the reacting species are consumed rapidly. As time progresses, gas velocities decrease because of pressure rise in the cavity (see Fig. 4b).

Following a relatively long period of inert heating, the AP and PBAA start to pyrolyze when the propellant surface temperature becomes sufficiently high. The gasified species of oxidizer, fuel, NH_3 and $HClO_4$ diffuse away from the surface,
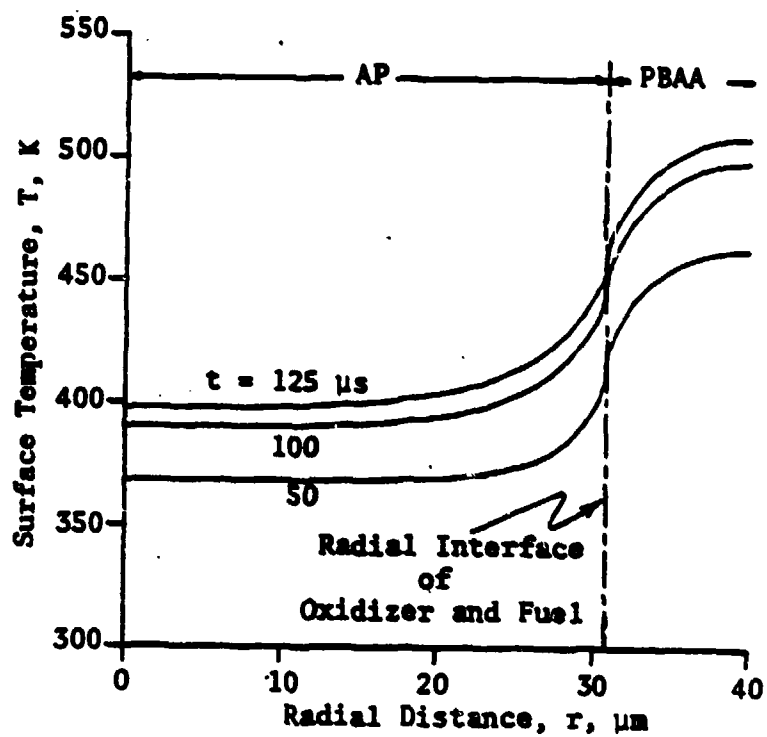
Fig. 7   Radial Variation of Surface Temperature at
Various Times (Average dP/dt = 120 GPa/s)
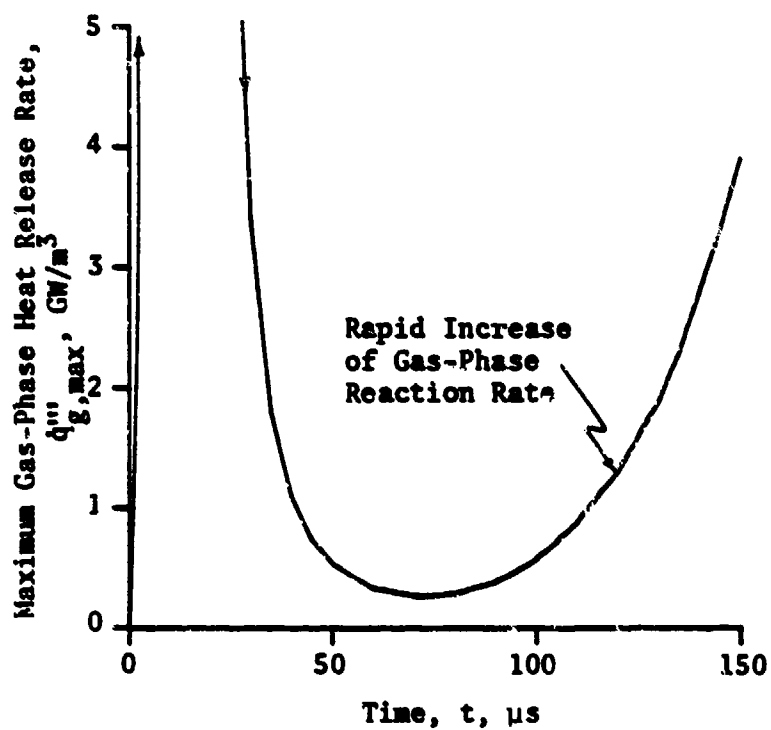
Fig. 8 Calculated Time Variation of Maximum Volumetric
Gas-Phase Heat Release (Average dP/dt = 120 GPa/s)

both axially and radially. As shown in Figs. 9 and 10, the concentration of fuel species is highest above the surface at $r = R_2$, where fuel surface temperature is highest (see Fig. 7). The fuel mass fraction decreases away from that location. The oxidizer concentration is highest at the AP-PBAA interface ($r = R_1$), as shown in Figs. 9 and 10, where the AP surface temperature is highest (see Fig. 7). As time progresses, the mixing of fuel and oxidizer species continues because of diffusion and convection. Since local temperatures are not high enough to support vigorous gas-phase reactions, the concentration of these species continues to increase as a result of accumulation.

As the pressurization process continues, the temperature of the gas-phase continues to increase. At the same time, there is an accumulation of fuel and oxidizer species due to pyrolysis of the propellant. When local concentrations and temperature reach suitable values, vigorous gas-phase reaction between pyrolyzed oxidizer and fuel species ensues (see Fig. 8). Ignition is defined as the attainment of high gas-phase reaction rates (see Fig. 8) and simultaneous high surface pyrolysis rates (see Fig. 4c and 4d).

2.3.4 Parametric Studies

The critical values used in ignition criteria (see Sec. 2.3.2) were obtained by matching the predicted ignition delay with experimental data for one case. Comparison between predicted ignition delay (for first three ignition criteria mentioned earlier) is shown in Fig. 11. It is clear that all three criteria correctly predict the experimentally observed trend[12] that ignition delay time is lower for higher pressurization rate. The last two criteria also show the same trend.

Predicted ignition delay time shows a greater dependence on the choice of ignition criteria at lower pressurization rates. The criterion based on zero velocity (IC 3) or critical burning rate (IC 2) results in a lower ignition delay
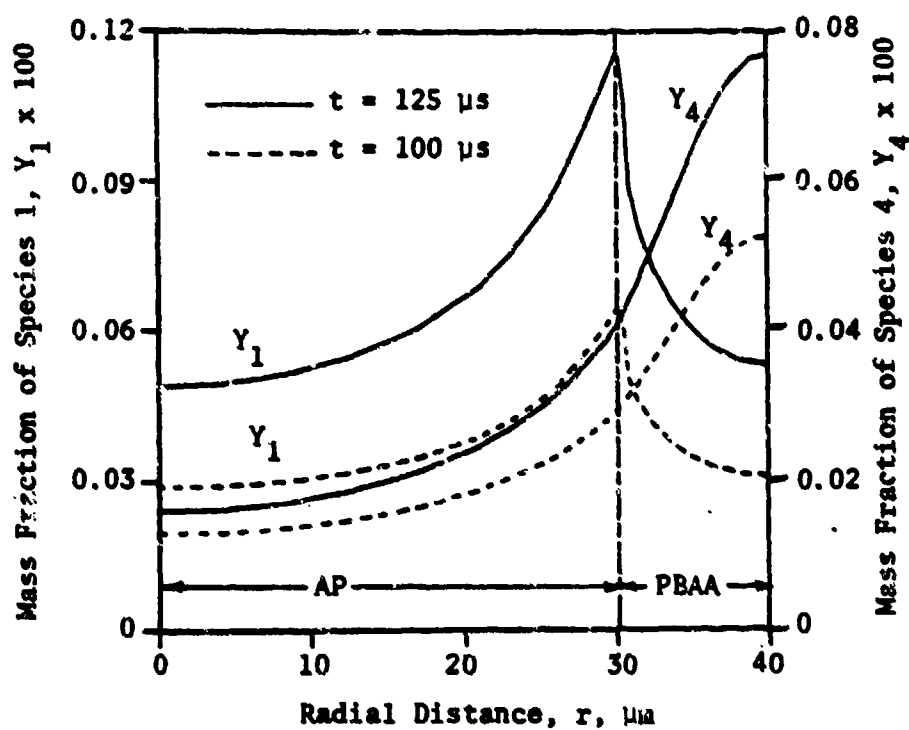
Fig. 9   Radial Variation of Oxidizer (Y_1) and Fuel (Y_4)
Species Mass Fraction Near the Solid-Gas Interface
at Two Different Times (Average dP/dt = 120 GPa/s)
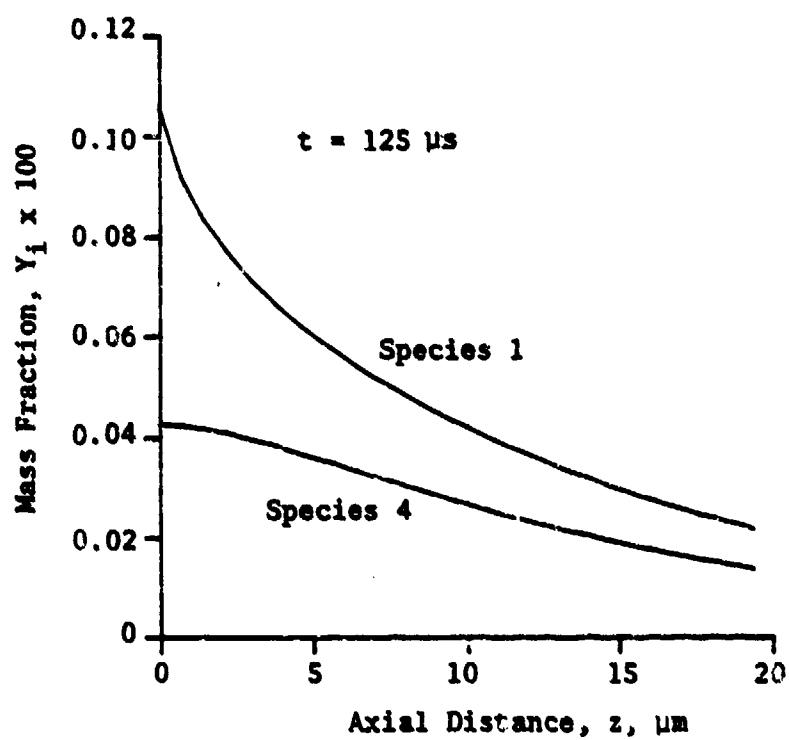
Fig. 10 Axial Distribution of Oxidizer (Y_1) and
Fuel (Y_4) Species above AP/PBAA Interface
($r=R_1$) (Average dP/dt = 120 GPa/s)
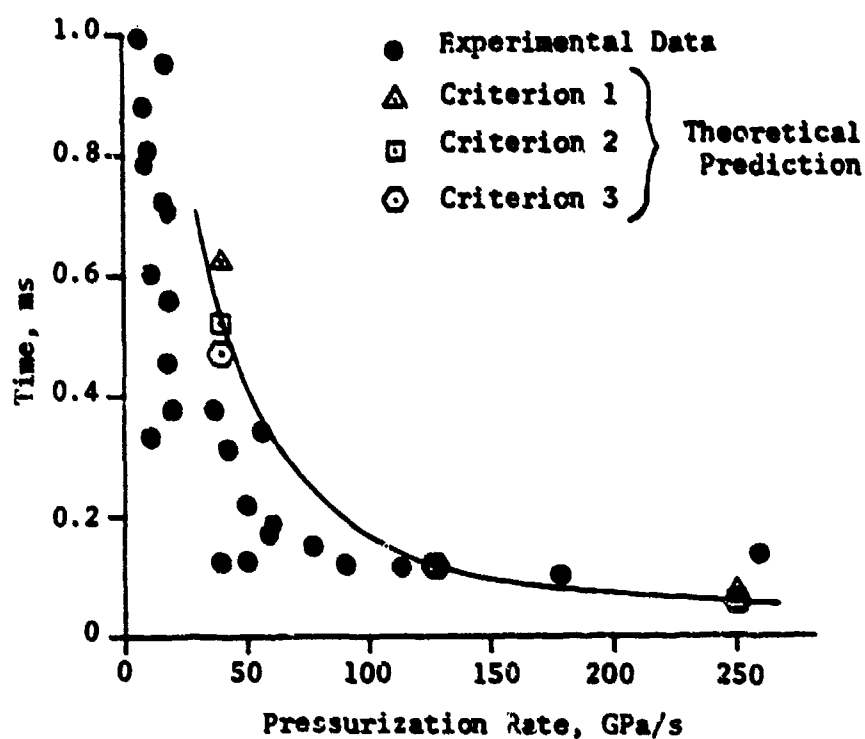
Fig. 11 Comparison of Measured and Predicted Ignition Delays Using Different Ignition Criteria Based Upon the Attainment of: (1) $\dot{q}'''_{max}$, critical; (2) $r_{b,critical}$; and (3) zero axial velocity in the gas phase at a specified location

time than that based on gas-phase heat release (IC 1). This is reasonable because at a lower pressurization rate, the gas-phase temperature increases at a slower rate; therefore, the time lag between significant pyrolysis and the attainment of the critical gas-phase reaction rate is longer. Theoretical results overestimate the ignition delay time at lower pressurization rates and slightly underestimates the ignition delay time at higher pressurization rates (see Fig. 11); this may be caused by approximate values of chemical kinetics constants used in the computation. Overall, predicted results are in reasonable agreement with the measured data.

Another possible ignition criterion that can be used, but was not employed for results presented in this report, is the appearance of an abrupt rise (spike) of the surface temperature (see Fig. 12) and the gas-phase temperature adjacent to the radial oxidizer-fuel interface. The spike occurs because of exothermic reactions on the AP side of the interface and endothermic reaction on the PBAA side. This spike results in both high pyrolysis rate at $r \approx R_1$ as well as pronounced gas-phase reaction rate near the circumference of the interface region. As evident from Fig. 12, the spike occurs at a later time than the onset of ignition based upon previously mentioned ignition criteria. However, the predicted trend of ignition delay will not be influenced by the selection of this ignition criterion.

It should be noted the predicted surface temperature at the onset of ignition is about 450 K which is considerably lower than that observed for steady-state burning. This is reasonable because of the time lag between the onset of ignition and steady state burning. If the program is allowed to run further in time, until steady-state conditions were reached, the surface temperature will approach the steady state value. This increased surface temperature can also be seen from Fig. 12.

Figure 13 shows the effect of AP-particle size on radial surface temperature distribution in the solid. As the AP-particle size is decreased, the radial temperature distribution becomes more uniform. This is reasonable because for small
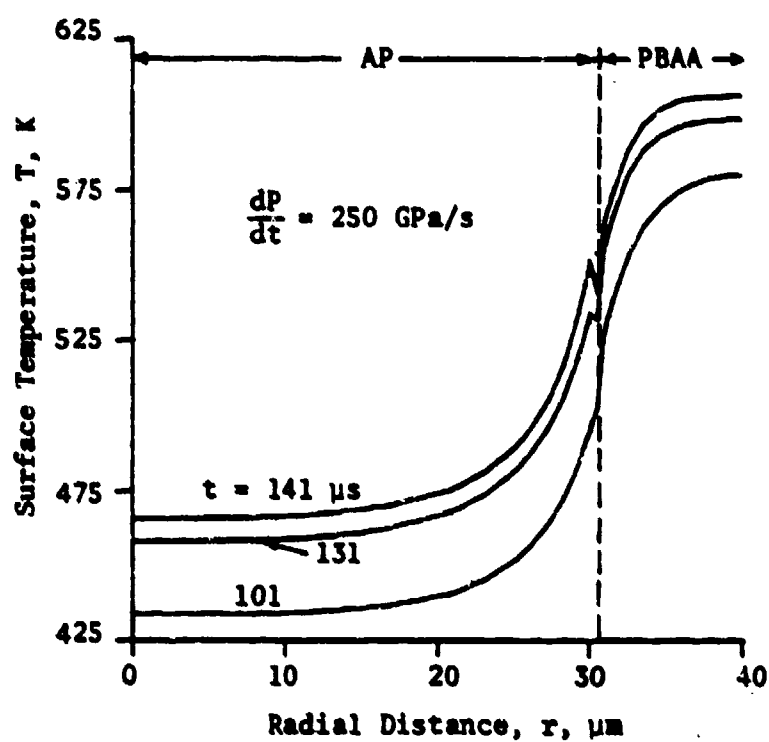
Fig. 12   Radial Variation of Surface Temperature
Showing the Appearance of Temperature
Peaks near Oxidizer-Fuel Interface
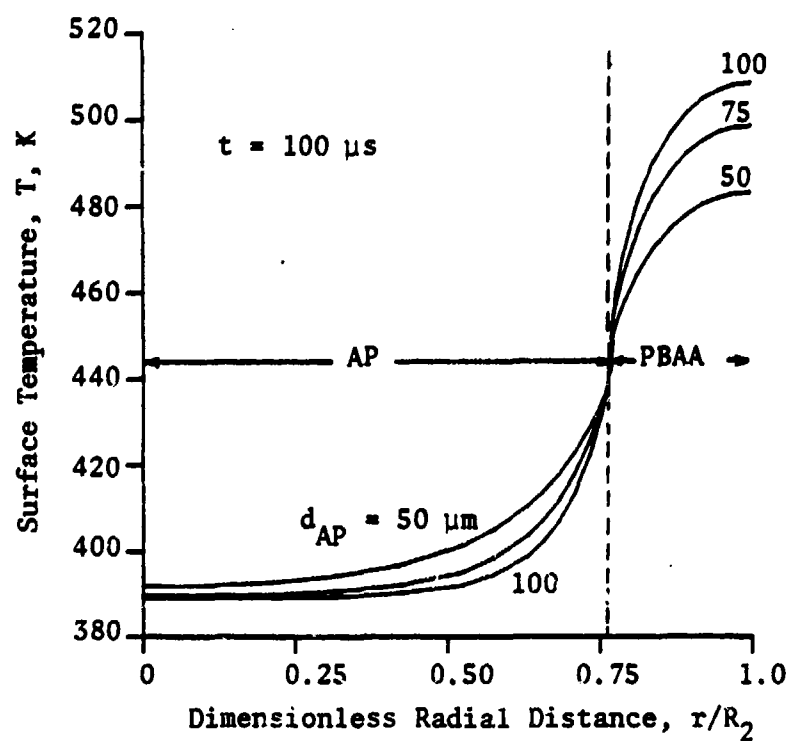
Fig. 13 Effect of AP Particle Size on Radial Variation of
Surface Temperature (Average dP/dt = 120 GPa/s)

particle size lateral heat conduction is more pronounced. In the limiting case, as the AP-particle size becomes vanishingly small, the temperature distribution will be uniform. Ignition criteria based upon AP burning rate (IC 2) or zero gas-phase velocity (IC 3) will result in lower ignition delay time for smaller AP particle size because for smaller particle size surface temperature on AP is higher. On the other hand, since the surface temperature on PBAA is lower for smaller AP particle size, the adjacent gas-phase temperature is lower than that for larger particle. Since pyrolyzed oxidizer species can diffuse readily to the higher temperature region over PBAA surface, the maximum rate of gas-phase heat release occurs there. As a result, for smaller AP particles, the ignition criterion based upon maximum gas-phase heat release (IC 1) will show longer ignition delay time, which is opposite to that predicted by the other two criteria (see Fig. 14). However, the predicted ignition delay times appear to be relatively insensitive to the oxidizer particle size. Since predicted ignition delay times are more strongly dependent upon the properties of fuel and oxidizer as well as the chemical kinetic constants, no conclusions can be drawn at this time as to the effect of oxidizer particle size on ignition delay.
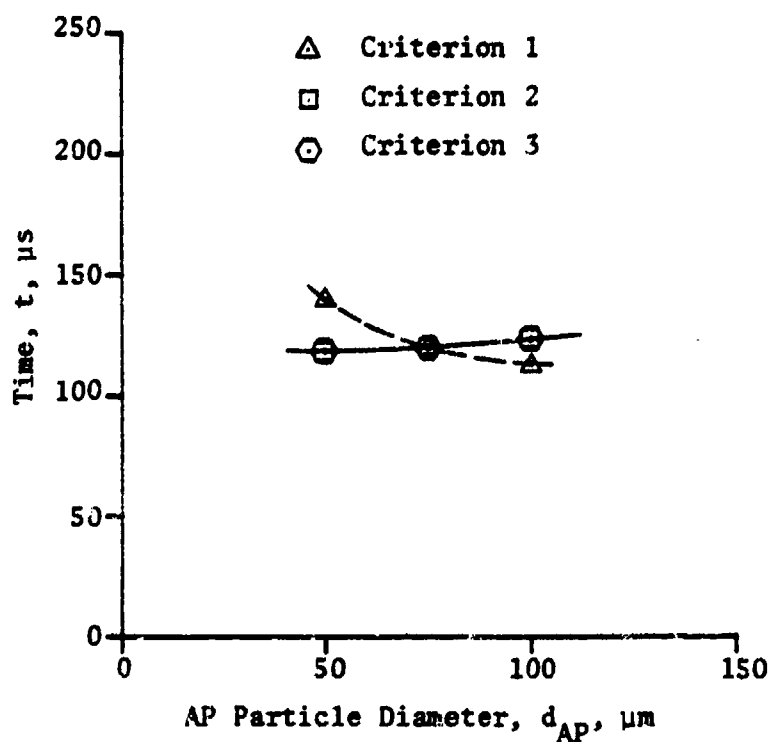
Fig. 14 Predicted Effect of AP Particle Size on Ignition Delays Using Different Ignition Criteria Based Upon the Attainment of: (1) $\dot{q}'''_{max,critical}$; (2) $r_{b,critical}$; and (3) zero axial velocity in the gas phase at a specified location. (Average dP/dt = 120 GPa/s)

III. INVESTIGATION OF PROPELLANT CRACK PROPAGATION

3.1 Experimental Observations of Crack Propagation in Burning Solid Propellants

At present, there is a lack of experimental and theoretical knowledge in the area of solid propellant grain fracture during motor firing. This technological deficiency becomes more acute when narrowing the field to grain fracture under rapid pressurization and burning conditions. This area is of special interest to investigators of rocket motor grain integrity, where high-speed crack growth and propellant fragmentation may provide enough additional burning surface area to enhance the possibility of deflagration-to-detonation transition (DDT) in solid propellant rocket motors.

In the past, numerous studies, based purely on solid mechanics considerations, have been conducted to investigate crack propagation. Despite the fact that there is no experimental evidence to support the validity of applying results of inert propellant crack propagation studies to live propellants under burning conditions, virtually all previous studies have employed inert propellants in non-burning environments. It is therefore apparent that an investigation of crack propagation under burning conditions would provide useful data to interpret the mechanism of crack propagation in a combusting environment.

An investigation was undertaken to help bridge this technological gap. Specific objectives of this study were:

1. To develop an experimental technique to study crack propagation in a composite solid propellant under burning conditions.

2. To measure crack propagation velocities in solid propellant samples.

3. To observe any abnormalities of the propagating crack.

4. To study the effects of chamber pressure and pressurization rate on crack propagation velocities.

5. To compare burning crack propagation results with experimental data and theoretical results of inert propellant crack propagation studies.

3.1.1 Experimental Setup

Crack propagation tests were conducted with a windowed chamber; the schematic diagram of the test rig is shown in Fig. 15. A propellant sample, with prefabricated crack, was internally pressurized by a small driver motor which produced high-temperature and high-pressure gases. The propellant sample configuration allowed for significant displacement of the crack walls, resulting in high stresses and strains at the crack tip which in turn led to crack propagation.

Figure 16 presents a schematic diagram of the driving motor used for hot gas generation. An electric primer (FA 874) was used to ignite the booster propellant and the igniter charge. The product gases flowed through a multiperforated nozzle into the main chamber, causing ignition, flame spreading, and mechanical deformation of exposed internal crack surfaces. The continued pressurization of the crack cavity is dominated by the output mass and energy fluxes of the driving motor. Using this apparatus, it is possible to obtain pressures up to 50 MPa (approximately 7000 psi), and pressurization rates in the order of 100 GPa/s (approximately 10^6 atm/s). For tests conducted in this study, pressurization rates ranged between one and ten GPa/s.

Figure 17 is a photograph of a typical propellant sample, mounted in a chamber. The sample was machined to a desired geometry and a uniform thickness. A 3 mm deep slit was cut with a sharp razor blade to help initiate crack growth. The propellant used was 73/27 AP/HTPB with 200 μm AP. Once the sample was installed in the chamber, a plexiglass window assembly was bolted on, slightly compressing the sample between the rear wall of the chamber and the window.

A block diagram of the data acquisition system used in the study is shown in Fig. 18. Pressure measurements were made at two locations in the main chamber (one at the crack entrance and the other in the crack-tip region) by piezoelectric transducers. Signals from the transducers were amplified through a charge amplifier

Pressure Transducer Ports

Propellant Sample

Driving Motor

Plexiglass
Window
Assembly
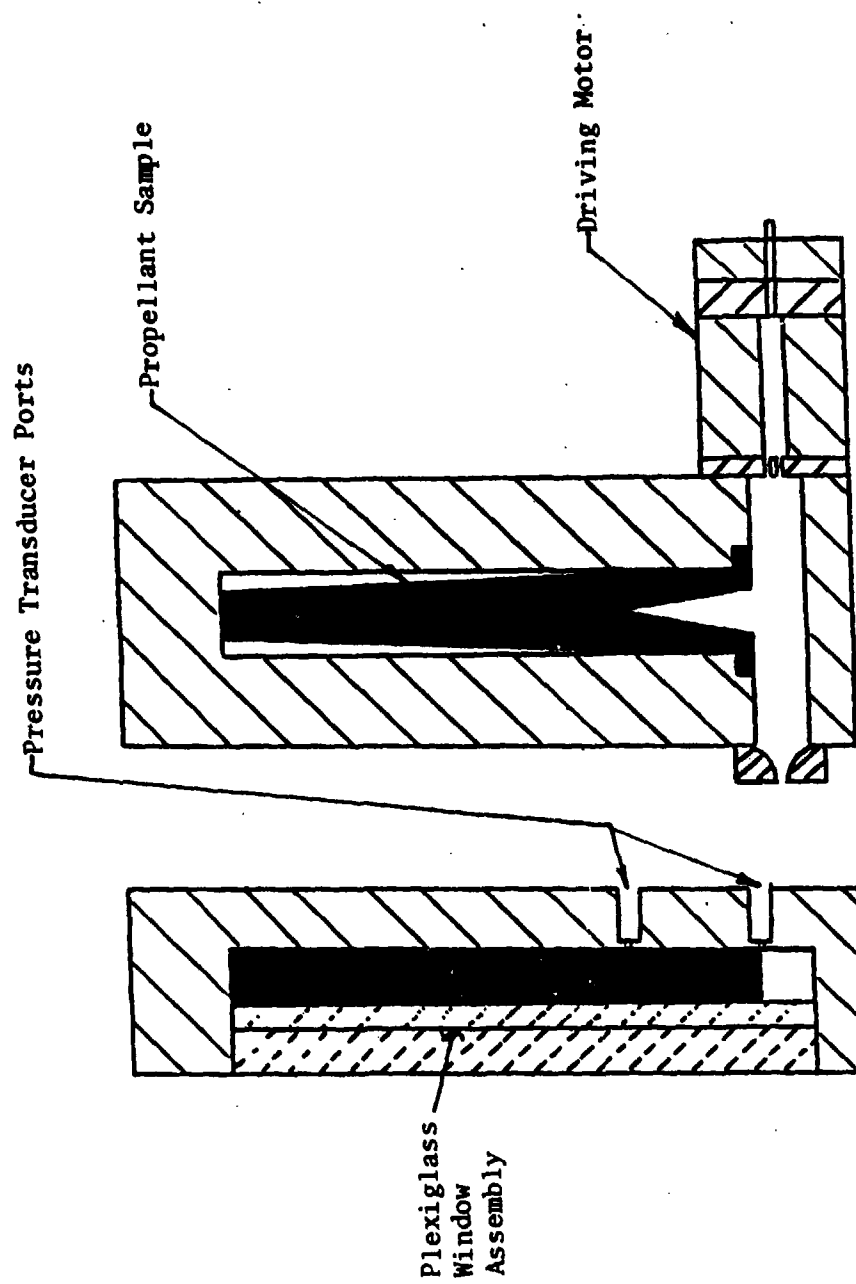
FIG. 15 SCHEMATIC DIAGRAM OF CRACK PROPAGATION CHAMBER
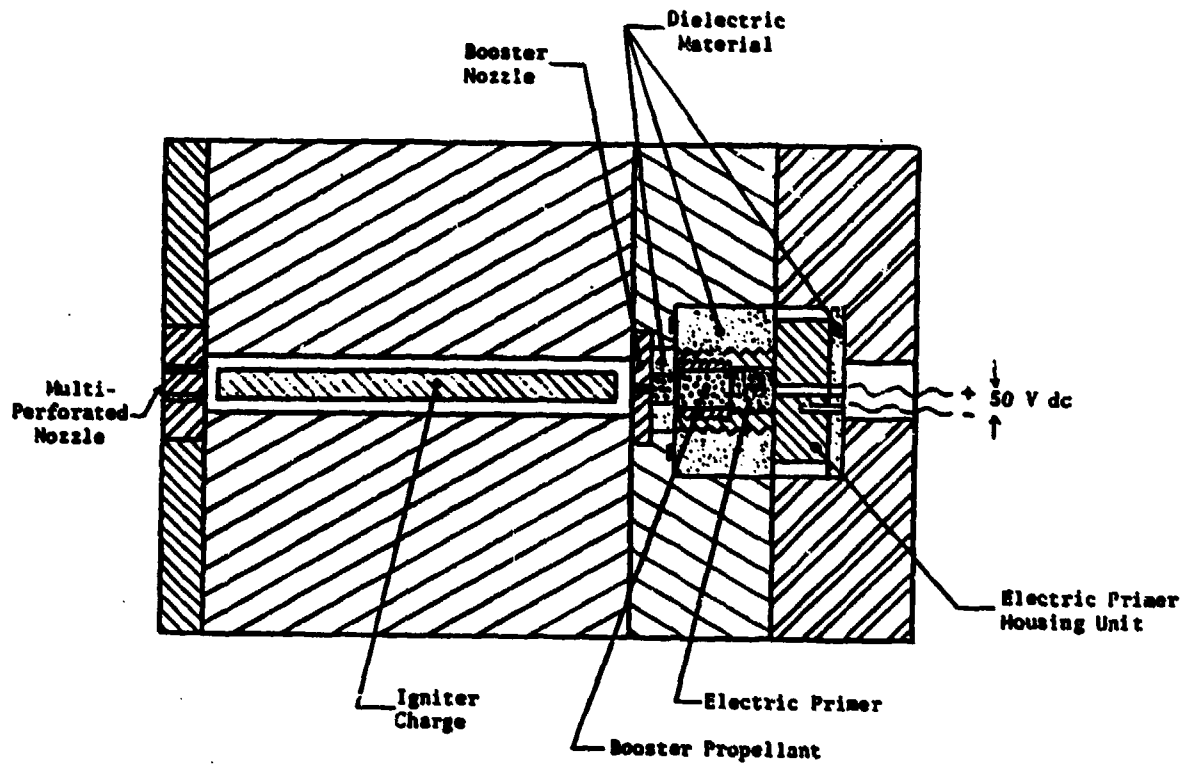
FIG. 16 SCHEMATIC DIAGRAM OF DRIVING MOTOR
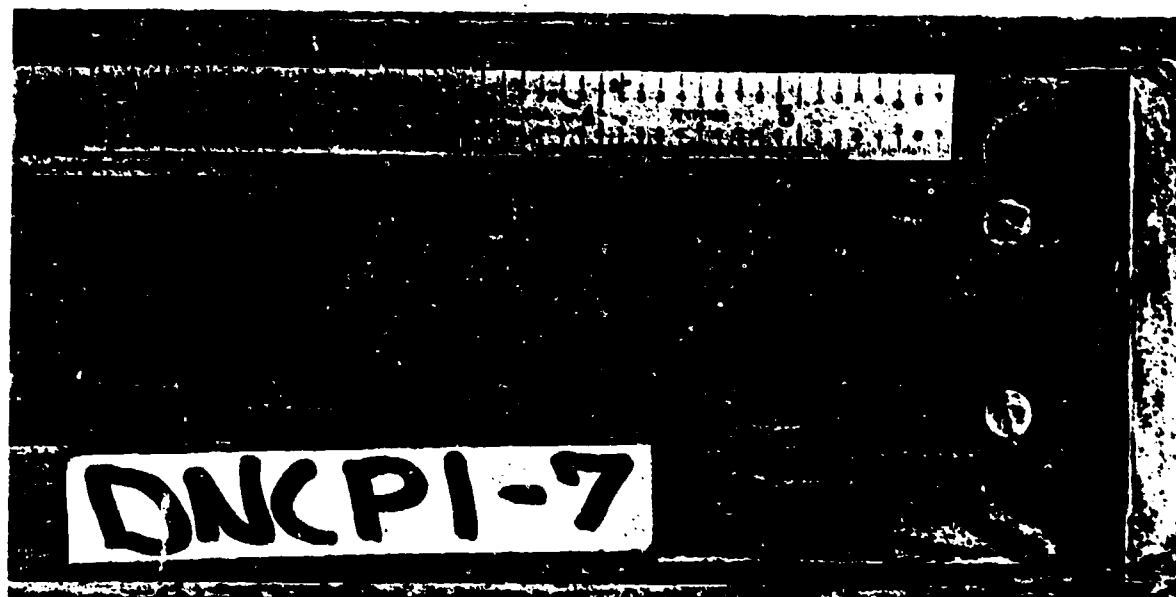
Fig. 17   Photograph of Propellant Sample Mounted
in Crack Propagation Test Chamber
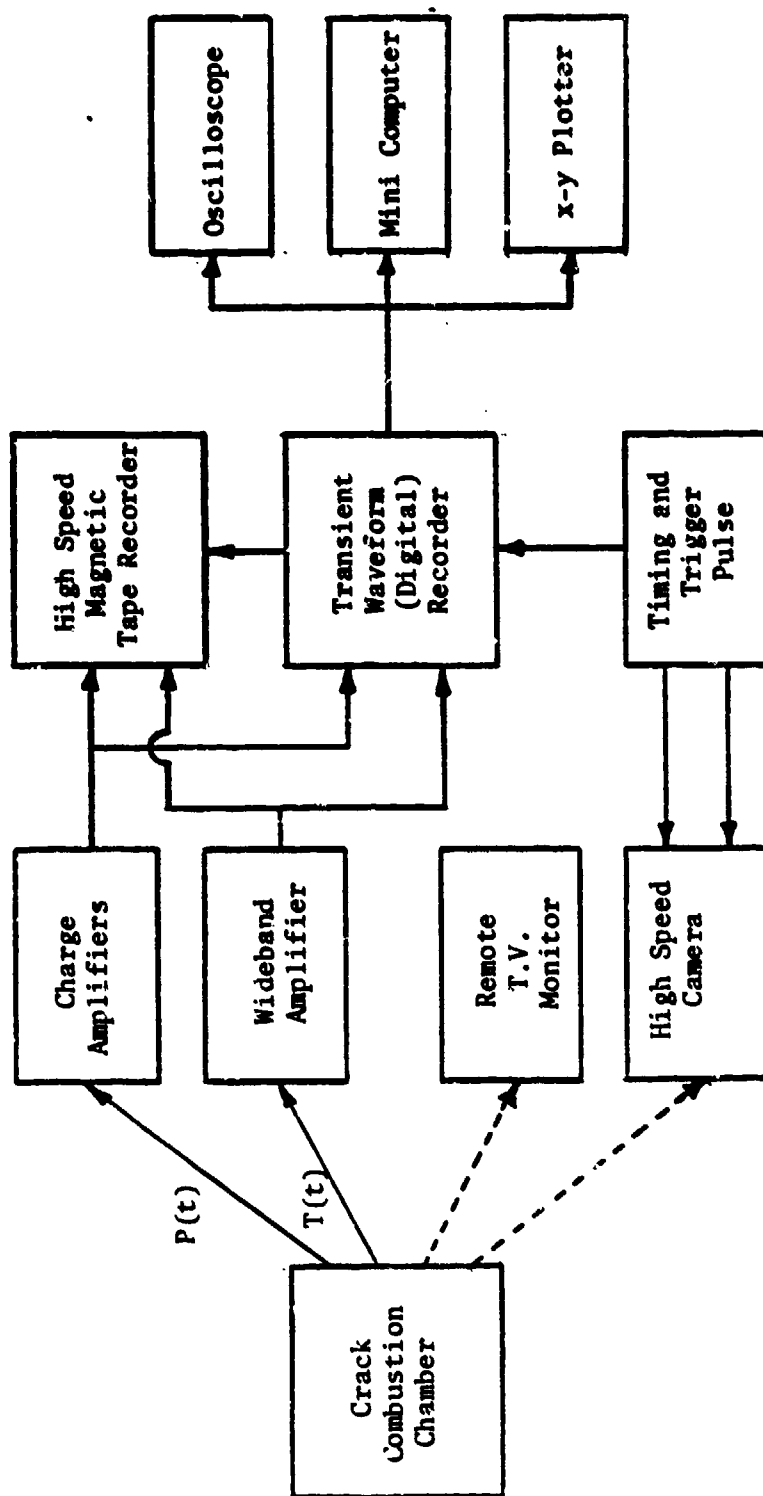
FIG 18 BLOCK DIAGRAM OF DATA ACQUISITION SYSTEM

before recording on the transient waveform recorder and the high-speed magnetic tape recorder. A visual record of the event was made with a 16 mm Hycam movie camera, using a 35,000 pps filming rate.

3.1.2 Experimental Results

Several variables were considered important to the outcome of the experiments: the sample's material properties, geometry, and initial temperature; the exit nozzle size; and the pressurization rate controlled by the efflux from the driving motor. Test results presented in this report include only effects of pressurization rate; other variables were held constant.

A typical pressure vs. time trace is presented in Fig. 19. From the plot, it can be seen that during the time interval of measured crack growth (approximately 1 msec), the pressurization rate was approximately constant. Nearly constant pressurization rates were observed for all test firings, and this fact provided a convenient test parameter which was easily varied from test to test by adjusting the size of the igniter charge loaded in the driving motor.

The bulk of data obtained in each test was recorded by high-speed photography. A typical film record is shown in Fig. 20. Hot gases from the driving motor illuminated the crack cavity and outlined the crack walls. In this figure, each vertical column of light is the outlined crack at a different time. The event proceeds from left to right with a time interval of 29 μs between consecutive pictures.

After an initial period of irregular crack-tip displacement (first three pictures), the event shown in pictures 4-9 illustrates a typical mode I crack propagation with the crack-tip displacement in the vertical direction as expected. However, in picture 10, a dramatic change takes place in the propagation mechanism. A fan region of light emerges just above the crack tip, and is accompanied by a change in the geometry of the crack. The crack walls, up to this point, have displaced outward towards the chamber walls. However, near the crack tip, a small triange is formed, indicating
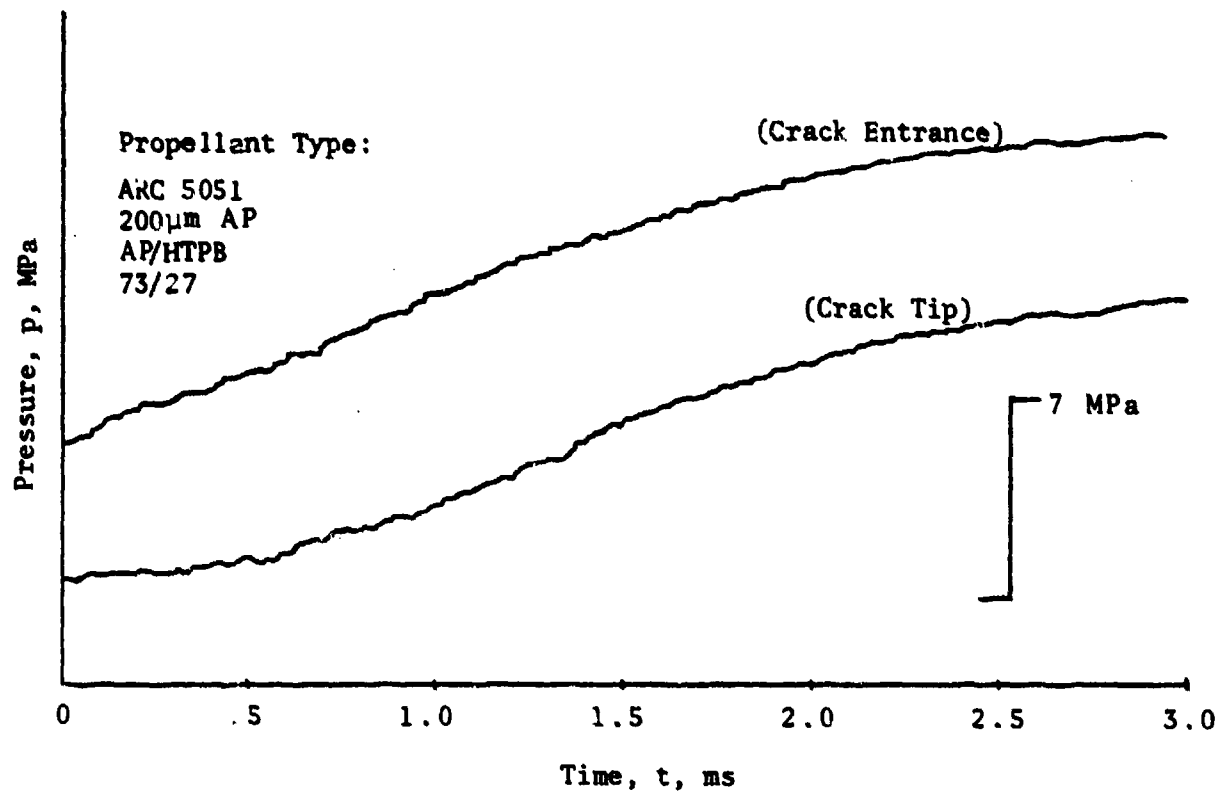
FIG. 19   PRESSURE-TIME TRACE FOR CRACK PROPAGATION TEST
(TEST NO. DNCP1-7; DP/Dt = 4×10^3 MPA/S DURING
MEASURED CRACK PROPAGATION)
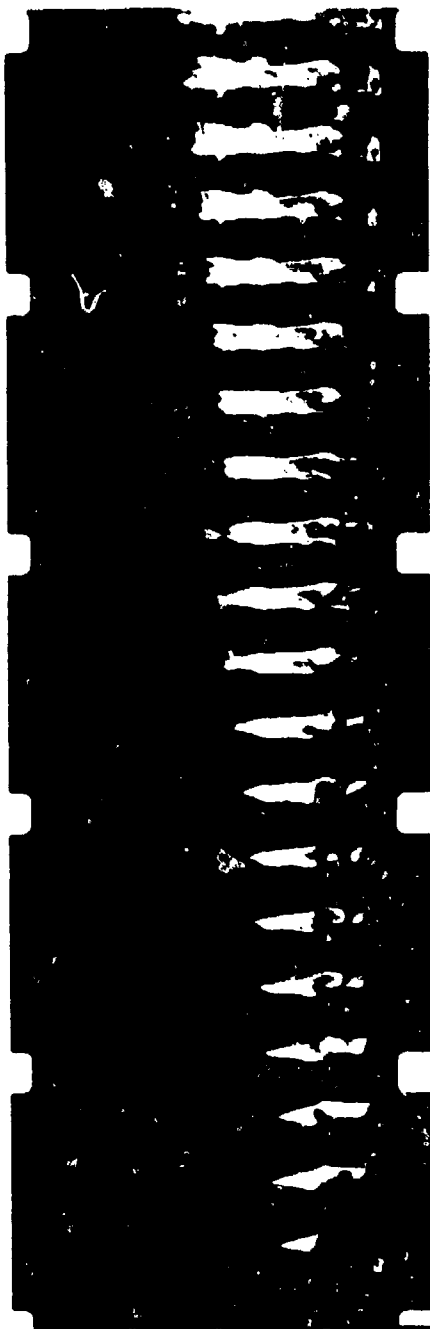
Fig. 20 Photograph of Crack Propagation in a Burning Solid Propellant with
High Pressurization Rate, dP/dt = 1.55 x 10⁵ atm/s (35,000 pps)

the existence of only one crack. After the fan region appeared, the crack walls become almost parallel, and the crack tip itself lost its definite triangular shape and became a jagged horizontal line. One explanation for the fan region and the corresponding change in crack geometry is the creation of micropores by the material fracture near the crack tip. This leads to branching of the crack, which allows crack walls to displace outward the square-shaped contour described above.

The crack-tip position for each test was plotted as a function of time. An example is presented in Fig. 21. If the tests were conducted in a non-burning environment, one could easily associate the crack-tip displacement with crack propagation velocity. However, in the case of a burning environment, mechanical displacement, material regression due to burning, and the possibility of flame spreading between the sample and window must all be considered. Burning rate calculations reveal that the effect of deflagration would only account for .1% of the displacement experienced, and therefore may be considerably negligible. The sample's vertical displacement at the crack tip due to pressurization was calculated using a finite element program. From this analysis, it was determined that the displacement could also be considered negligible when compared to the total displacement. The vagueness due to flame spreading above the crack tip can be eliminated by the interpretation of the film. While it is not obvious from the black-and-white reproductions of the photographs included in this paper, the actual geometry of the crack cavity can be identified in most cases by using a motion analyzer for close inspection of the films.

Once the displacement plot shown in Fig. 21 was established as the approximate crack propagation plot, crack velocities were obtained by a least-square fit. All tests revealed nearly constant crack velocities after a short initial period of irregular crack growth. These velocities ranged from 20 to 70 m/s. A major objective of this study was to determine the effect of pressurization rate on crack velocities.
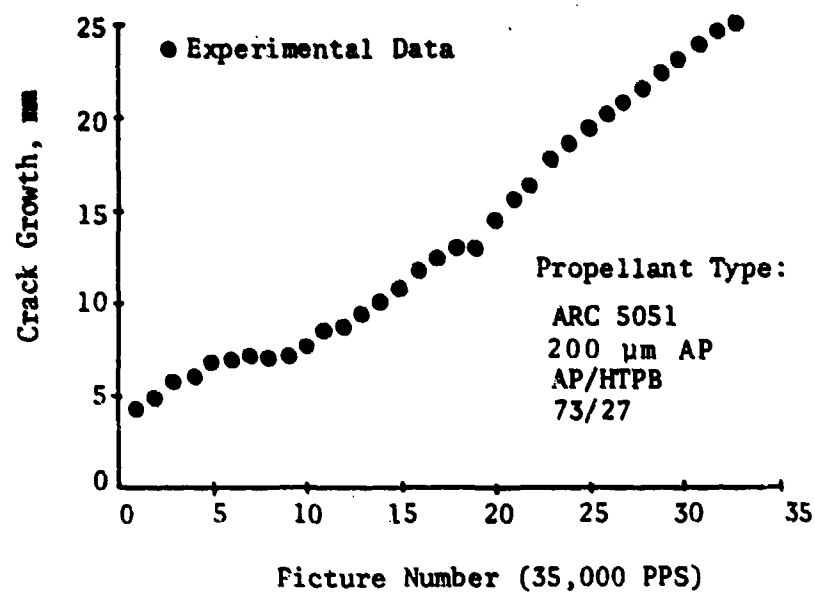
FIG. 21 MEASURED CRACK GROWTH IN A BURNING SOLID PROPELLANT

Since a constant velocity and pressurization rate was observed for each test, each experiment provided a data point for the plot presented in Fig. 22. This plot demonstrates a definite trend, i.e., higher pressurization rates result in higher crack velocities. The straight line on the plot represents the experimental correlation given below:

$$v_c \text{(m/s)} = .169 \ [\frac{dP}{dt} \text{(MPa/s)}]^{0.608} \tag{39}$$

It must be noted that at present this correlation has been developed for a specific propellant with a fixed initial geometry and temperature.

Another aspect of increasing pressurization rates is illustrated when comparing Figs. 20 and 23. Pressurization rates for the tests shown in Figs. 20 and 23 were 1.5×10^5 and 3.0×10^4 atm/s, respectively. At the lower pressurization rate, the crack-tip region maintained its original triangular shape with only small deformations, while the test conducted at the higher pressurization rate revealed a square crack shape with a ragged tip region, indicating crack branching. The geometric transformation was accompanied by an increase in combustion intensity (see Fig. 20). The pictures on the right side of Fig. 23 present an example of flame spreading across the face of the sample. In this case, it is possible · distinguish between the flame spreading and the triangular crack contour. The pictures in Fig. 20 on the other hand, show limited flame spreading and the clearly outlined square shaped crack.

3.1.0 Discussion of Results

A major obstacle which arises when comparing results of this study with contemporary theories of crack propagation in viscoelastic solids is the choice of correlation parameters. The quasistatic crack propagation model proposed by Knauss[20,21] and Schapery,[22] and experimentally verified by Knauss,[20] Francis,[23] and Langlois and Gonard[24] relates crack velocities in terms of stress intensity. Calculating the stress intensity for the geometry and loading conditions used in this
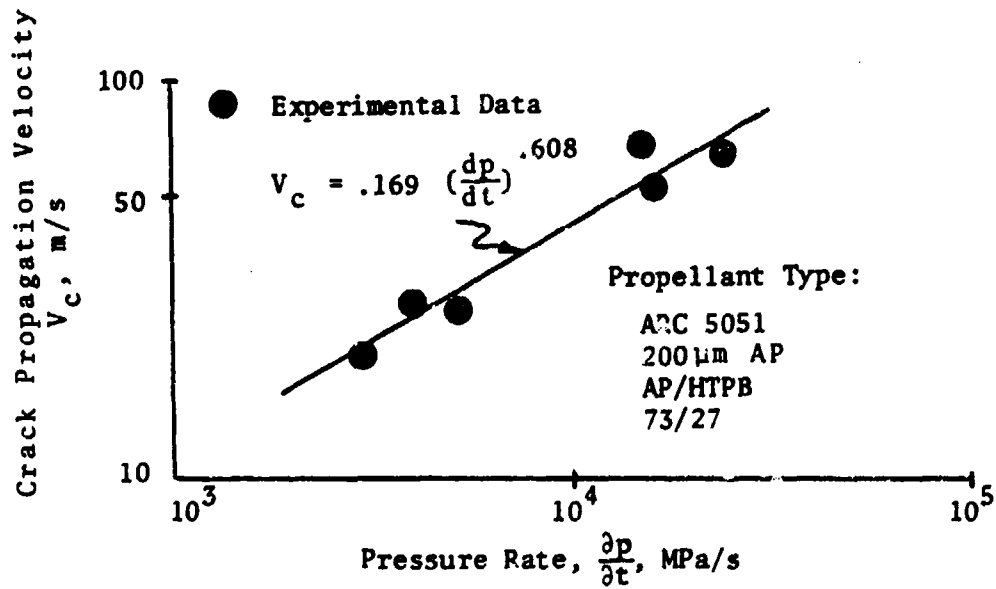
FIG. 22 MEASURED EFFECT OF PRESSURIZATION RATE ON CRACK
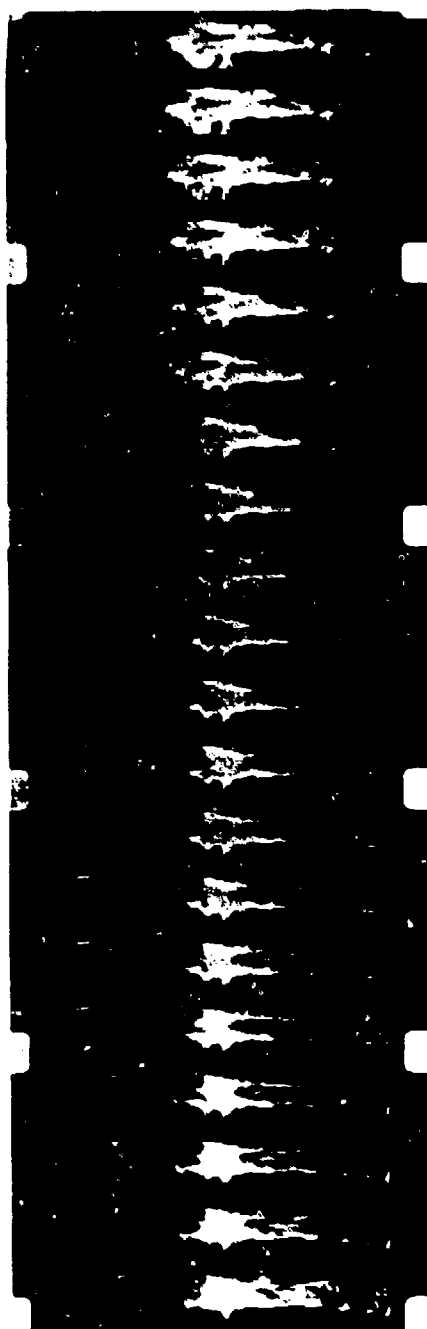PROPAGATION VELOCITY IN A BURNING SOLID
PROPELLANT CRACK

44

16

10

1
(Picture No.)

36

30

20

17
(Picture No.)
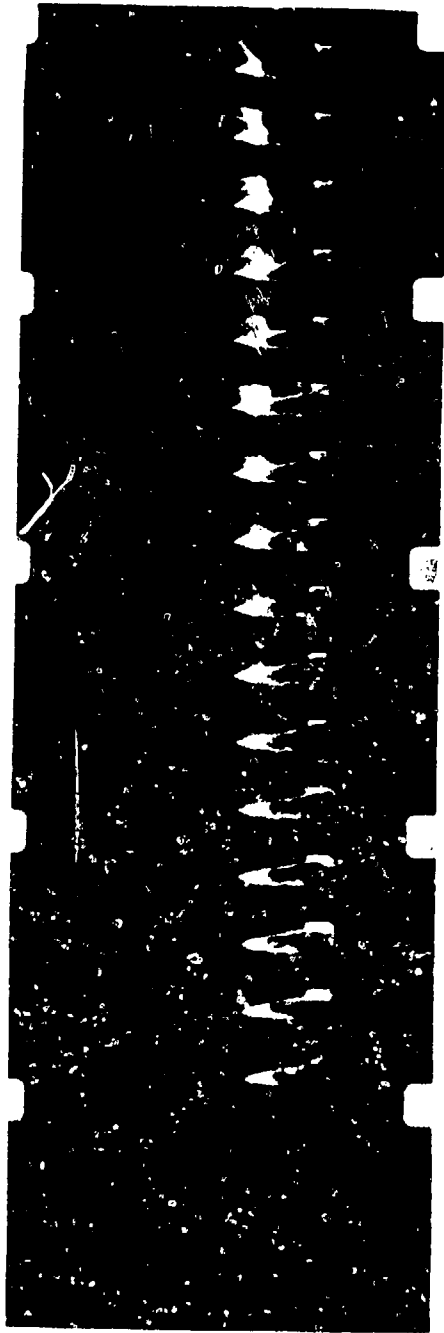
Fig. 23 Photograph of Crack Propagation in a Burning Solid Propellant with
Low Pressurization Rate, $dP/dt = 3 \times 10^4$ atm/s (35,000 pps)

study is complicated and uncertain. The geometry of the sample does not lend itself to classical elastic or viscoelastic solutions. In addition, the boundary conditions change as the sample's legs are compressed against the chamber walls. The effect of the hot combustion gases at the crack tip on the propellant's material properties is also unknown. However, it is possible to make a few realistic assumptions about the stress intensity at the crack tip. The sample exhibits failure at the tip almost immediately during the event at very low pressures (500 K Pa or less). As the load increases, more energy is made available to deform the crack walls, therefore increasing the stress intensity at the tip. During the pressurization and crack propagation interval, the stress intensity increases with pressure; however, the crack propagation velocity quickly reaches a terminal velocity. This implies that for the range of pressurization rates considered and the crack geometry tested, the crack velocity is independent of stress intensity. This phenomenon has been reported by Kim and Knauss,[25] Swanson,[26] and Gent and Marteny[27] in their studies of dynamic crack growth. Therefore, it is believed that the present burning crack propagation study is in the dynamic regime and cannot be described by the quasistatic model.

It is interesting to note that the measured burning crack propagation terminal velocity is between 20 to 70 m/s, which is of the same order as those reported by Swanson[28] and Gent[27] in inert propellants and rubber, respectively. Swanson reported maximum velocities of approximately 40 m/s, while Gent observed crack velocities of 80 m/s in specimens with no pre-imposed strains in the crack direction. Both Swanson and Gent proposed upper bounds to dynamic crack propagation rates based upon characteristic wave speeds in the material. Swanson selected the glassy Raleigh wave velocity as an upper bound to crack propagation velocity. He found that for inert propellants the maximum velocities measured were one order of magnitude below the Raleigh wave speed. Gent proposed that the crack propagation velocity in rubber was proportional to the velocity of sound in the material.

More specifically, the crack propagation velocity V_c is related to the speed of sound V_s by:

$$V_c = .3 \, V_s \tag{40}$$

Gent also noted that the speed of sound is strongly dependent on the state of strain in rubber.

Dynamic material properties for the propellant used in this study are not fully defined; however, typical values for similar propellants were assumed, and sample calculations were performed in order that comparisons could be drawn. One can approximate the speed of sound in a viscoelastic material using the formula given below:

$$V_s = \sqrt{E/\rho} \tag{41}$$

where E is the dynamic tensile modulus and ρ is the density of the material. Using Eq. (41), the calculated V_s is 205 m/s for a dynamic tensile modulus of 63 MPa and a propellant density of 1.49 gm/cc. E was determined from an experimentally derived plot of E as a function of loading time, and a maximum loading rate of 24,000 MPa/s was used. Using Eq. (40), V_c is found to be 62 m/s. The actual crack propagation velocity measured for the maximum pressurization case was 68 m/s, which is close to the calculated value obtained from Eqs. (40) and (41). Even though there is some agreement, the method of calculating the speed of sound is crude, since V_s depends on the state of strain in the sample, as pointed out by Gent, and may also be affected by the geometry of the sample and the hot gas environment.

At present, the strong dependence of crack propagation velocity on pressurization rate (as illustrated by the correlation given in Eq. 39), is not fully understood. One explanation for this dependence is the transition of the material towards a more brittle state as loading rate is increased. Using Eqs. (40) and (41) and an experimentally derived expression relating the dynamic tensile modulus to pressurization rate, one can examine the approximate effect of the material transition on

crack propagation velocities. For a similar composite solid propellant, it was determined that E was proportional to dp/dt raised to the .07 power in the range of pressurization rates tested.

$$E \propto (\frac{dp}{dt})^{.07} \tag{42}$$

Using the equation for the speed of sound in a material [Eq.(41)], and assuming that $V_s \propto V_c$ [Eq.(40)], one can derive the following proportionality relationship between V_c and dp/dt:

$$V_c \propto (\frac{dp}{dt})^{.035} \tag{43}$$

This relationship shows a weak dependence of crack propagation velocity on loading rate, due to the transition of the material towards the glassy state; however, the measured dependence was much stronger, as shown by

$$V_c \propto (\frac{dp}{dt})^{0.608} \quad \text{(from Eq. 39)} \tag{44}$$

The difference between the exponents in Eqs. (43) and (44) suggests that the material property transition is not the sole reason for the increase of crack propagation velocity with pressurization rate.

3.2 Design and Fabrication of New Crack Propagation Test Chamber

A new combustion chamber is designed (see Fig. 24) in order to investigate the phenomena of crack propagation and branching in a burning solid propellant crack under more suitable and reliable conditions. After considering the limitations and the problems experienced during the previous experiments, the following design criteria were incorporated into the new test rig.

3.2.1 Increased Chamber Width

a. To allow a greater flexibility of sample geometry.

b. To decrease the influence of reflected compression waves from the chamber walls.
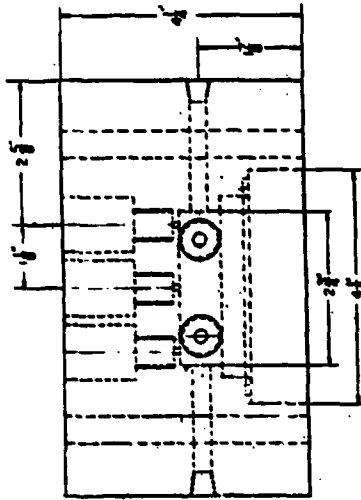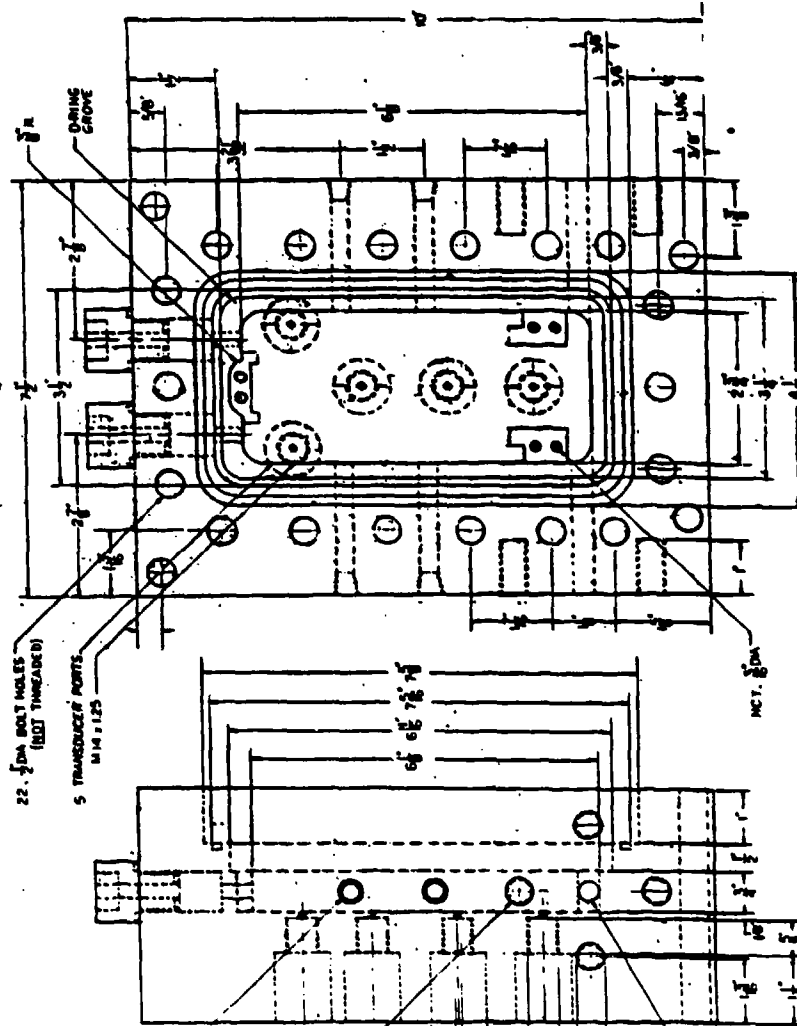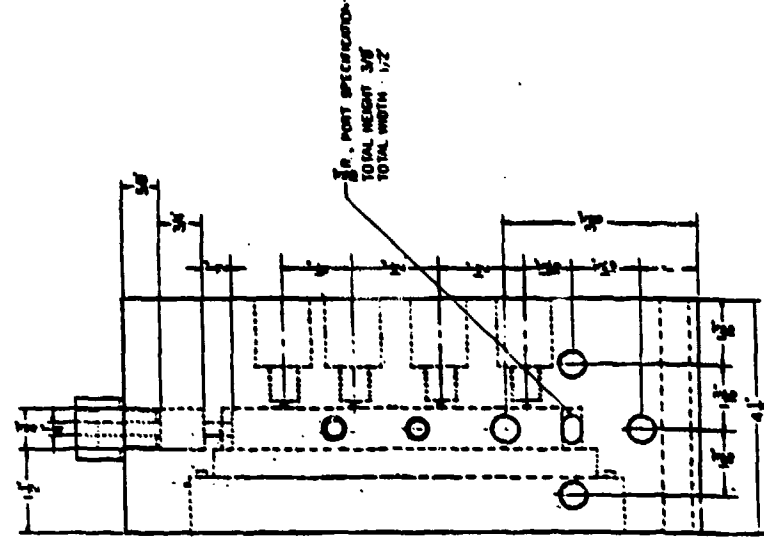
Fig. 24 Crack Propagation Test Chamber Design

c. Two provide for a longer period of crack growth and therefore increase the quantity of data recorded for each test.

3.2.2 Increased Chamber Depth

a. To house the igniter assembly in the main body of the crack propagation chamber. By so doing the hot gas passage is located away from the interface between main body and window retainer piece; and therefore any possible leaks can be prevented.

b. To allow for thicker plexiglass windows for strengthening the test chamber and also to reduce the possibility of flame penetration between the propellant sample and sacrificial window.

3.2.3 New Instrumentation and Lighting

a. Two different locations of feedthroughs for mounting break wires or thermocouples to detect the arrival of hot combustion product gases and instantaneous crack tip front.

b. Additional pressure transducer ports above the initial crack tip.

c. External lighting by using a light source with fiber optics to illuminate the sample surfaces not in contact with combustion gases. This provides information on the outer boundaries of the propellant sample.

d. Gas sampling ports are provided for collecting and analyzing combustion product gases.

3.2.4 Strength Considerations

A detailed stress analysis was done for a chamber pressure of 5000 psi to determine the chamber wall thickness, plexiglass window thickness and the required number and size of bolts for retaining the window assembly, igniter system and the exit port.

A thick (3-1/2") window retainer plate with two separate viewing areas, instead of a single long opening, was designed in order to prevent window buckling and retainer plate warpage. The front views of the window retainer plate is shown in Fig. 25.

3.2.5 Test Chamber Fabrication

304 stainless steel material was chosen for the test chamber fabrication in order to resist corrosive effects of combustion product gases. The test chamber components are being constructed at Houtz Instrument and Machine according to detailed mechanical drawings and the fabrication is expected to be finished by November 30, 1982.

3.3 Finite Element Analysis of Propellant Sample Used in Crack Propagation Studies

A stress analysis of the propellant sample was performed in order to gain some insight into the mechanical behavior of the sample material under constant internal pressurization of the crack cavity. Several factors make this analysis complicated and therefore certain assumptions were made to simplify the problem and reduce computation time. These assumptions reduce the accuracy of the results; however the analysis provides a qualitative picture of the strain and stress distributions in the sample before crack propagation.

The finite element grid for the model was generated on an interactive mesh generation program (STAB). The sample was considered to be symmetric about the crack axis and a finite crack radius of 1.78 mm (.07 in.) was used. The boundary conditions on the crack sample for the finite element program are shown in Fig. 26.

The model was solved using a non-linear finite element code (ABAQUS). The assumptions and options used are listed below:

1. An elastic analysis was used; however, the sample's viscoelastic behavior was approximated by using the relaxation modulus, corresponding to the

Fig. 25 Front View of the Window Retainer Plate
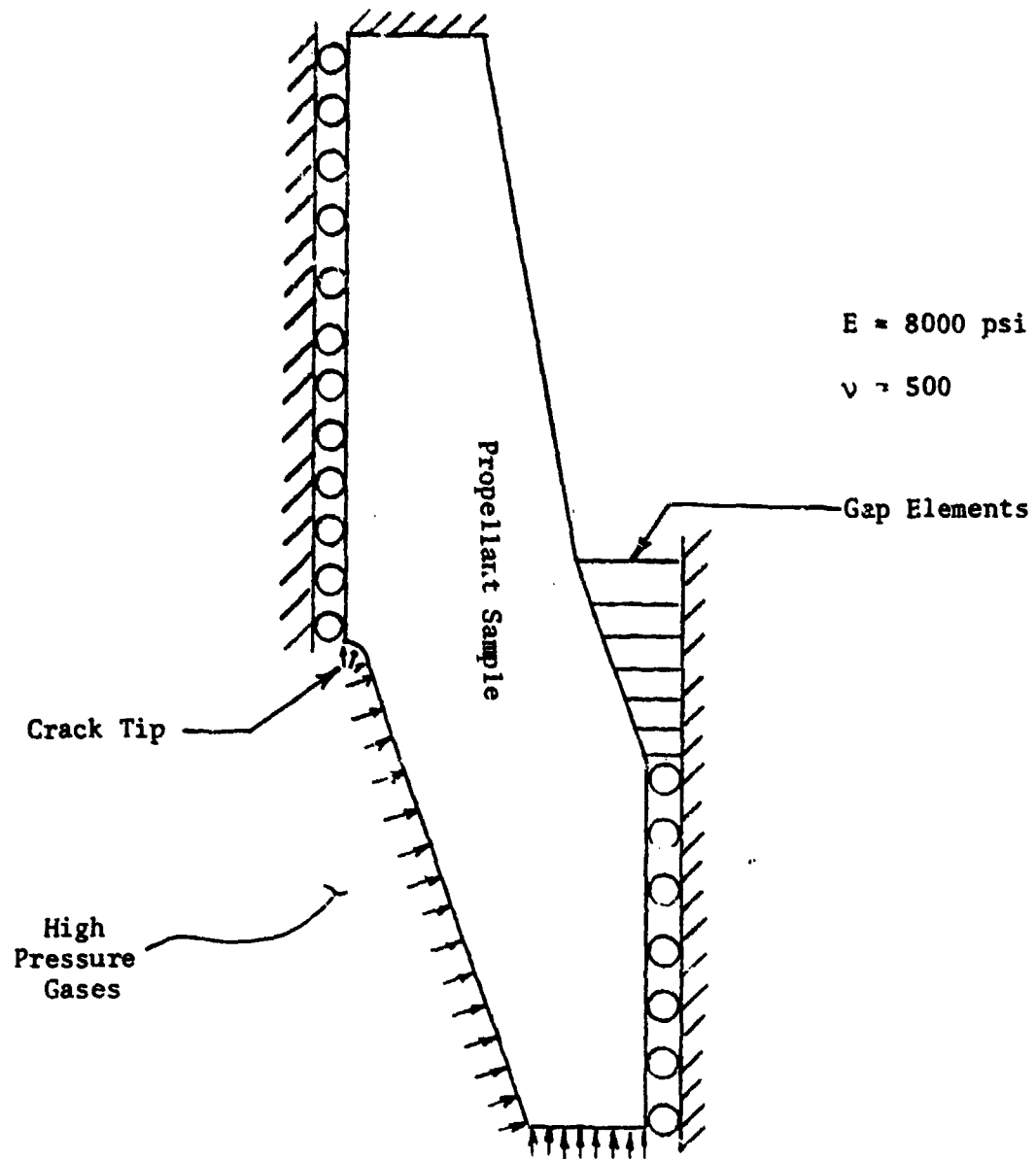
Fig. 26 Boundary Conditions on the Crack Sample for
Finite Element Program

test pressurization rate and initial temperature, in place of the elastic tensile modulus. This is a common procedure used in solid propellant grain deformation analysis.[29]

2. The program allowed for incompressible materials and a realistic poisson ratio of .5 was used for the propellant sample.

3. A non-linear large deformation analysis was performed. This option is needed since the observed mechanical deformation is quite significant.

4. Non-linear boundary conditions were modeled using gap elements between the sample and the chamber wall. This allows for unrestricted displacement of the sample lags until the outer surface is in contact with the chamber wall.

5. This preliminary analysis did not allow for the propagation of the crack tip since ABAQUS does not have this capability. In spite of this fact the solution obtained are extremely useful for the understanding of the mechanical behavior of the sample prior to fracture.

The finite-element stress analysis results are presented in Figs. 27 and 28. Figure 27 is a displacement plot where the dotted lines represent the initial location of the sample at initial pressure of 0.1 MPa and the solid lines represent the displaced elements at 5.17 MPa. It can be seen clearly from this figure that the mechanical displacement of the crack contour is significant; however, the initial triangular shape of the crack cavity is maintained. Figure 28 shows the contours of maximum principal deviatoric stress near the crack tip region. An interesting fact to note from this plot is that the maximum stress is located near the shoulder of the crack tip instead of at the apex of the crack. This is due to large deformations perpendicular to the crack axis. The result supports the observed transformation of the crack contour from initial triangular into a square shaped contour as discussed in Section 3.1.

DISPL.
MAG. FACTOR = 1.0
SOLID LINES - DISPLACED MESH
DASHED LINES - ORIGINAL MESH
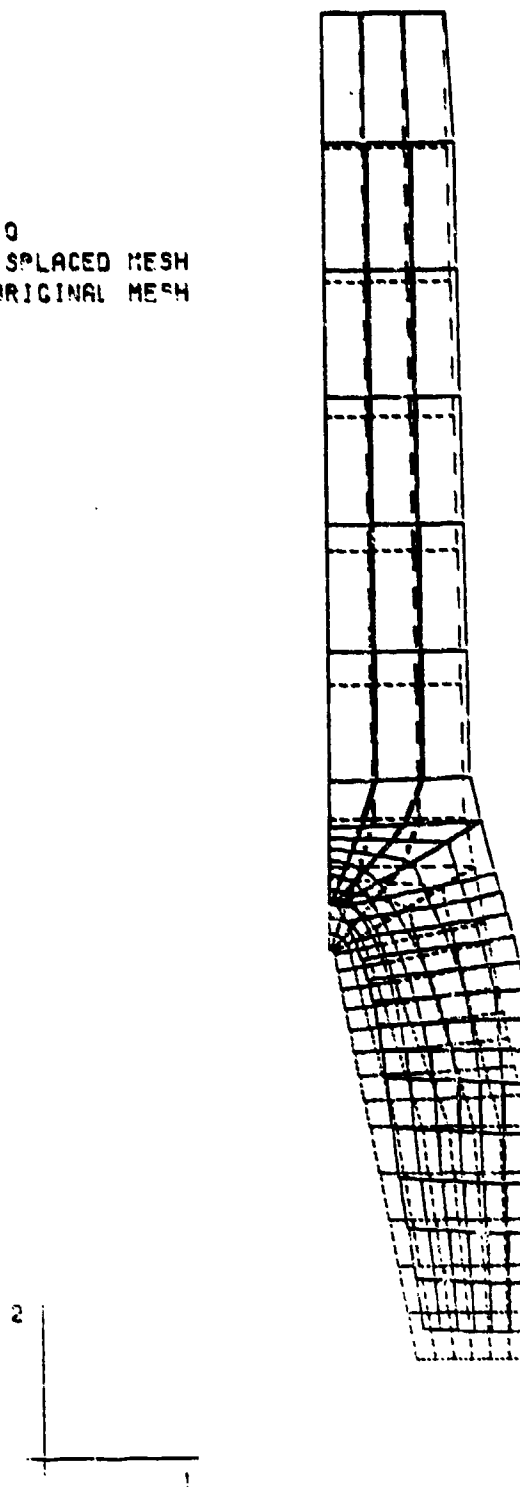
Fig. 27   Calculated Displacement of the Propellant Crack
Sample from Finite Element Program

```
MISES EQUIV. STRESS
I.D.   VALUE
 1     0.00  E  1
 2     400.00
 3     800.00
 4     1200.00
 5     1600.00
 6     2000.00
 7     2400.00
 8     2800.00
 9     3200.00
10     3600.00
11     4000.00
```
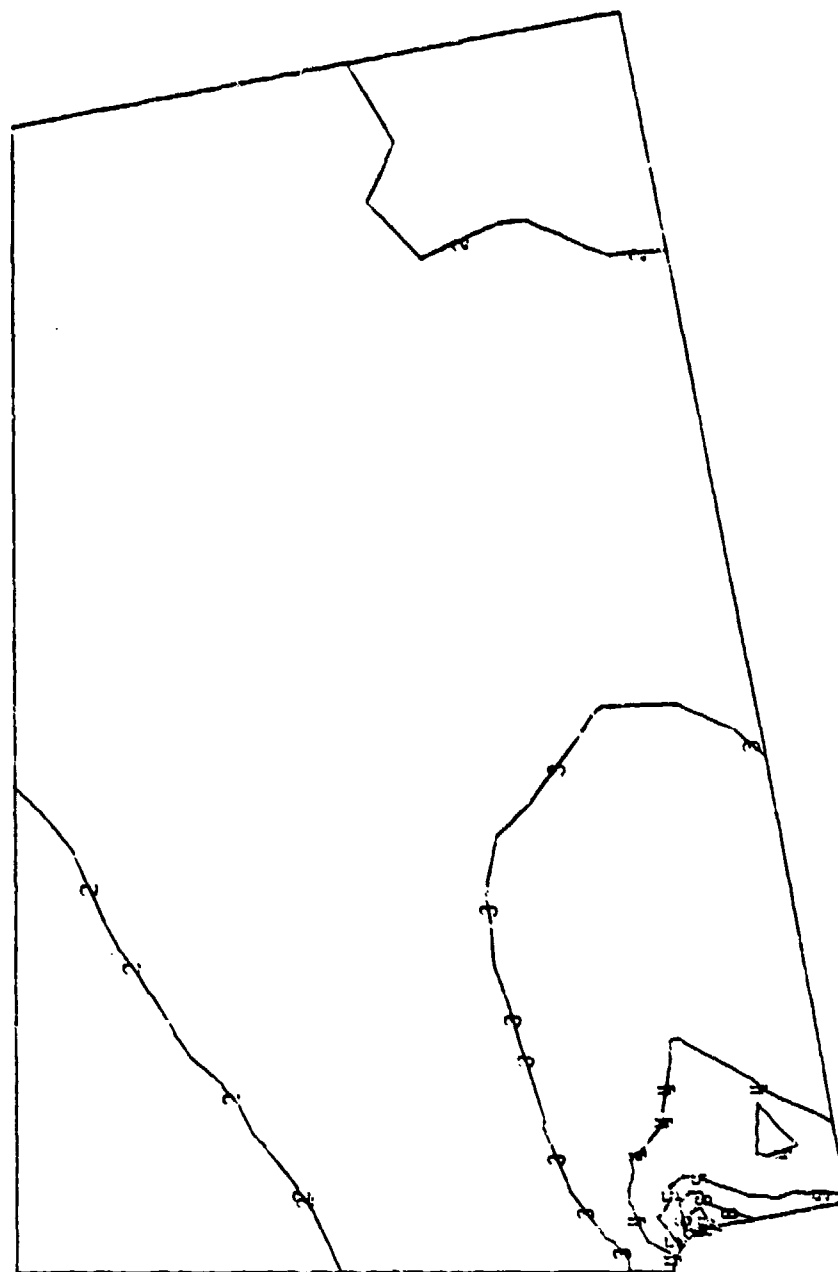
Fig. 28   Calculated Contours of Maximum Principal Deviatoric Stress Near the Crack Tip Region

IV. SUMMARY AND CONCLUSIONS

Some important observations and conclusions from the crack tip ignition study are summarized as follows:

1. A bright luminous zone behind the reflected compression wave was observed at high pressurization rates. Diagnostic experiments reveal that the luminous zone is caused by combustion of unreacted species from the igniter system.

2. Experimental results indicate that as the pressurization rate is increased, heat flux to the propellant surface increases and hence ignition-delay time decreases. No distinguishable effect of the crack gap width on the ignition process was evident for the range considered. Limited results obtained by using an aluminized propellant as the igniter show that the ignition-delay time is somewhat lower for higher flame-temperature igniter gases.

3. Calculated ignition delay times based on several criteria (namely, attainment of a critical volumetric gas-phase heat release rate, a critical pyrolysis rate, and zero axial velocity in the gas-phase near the propellant surface) are in agreement with the experimentally observed trend that ignition delay time decreases with increasing pressurization rate. Predicted values of ignition delay for lower pressurization rates showed greater dependence on the choice of ignition criterion.

4. The solutions revealed that the ignition process consists of the following sequence of events: (a) As pressurization begins, the gas-phase temperature starts to rise, the unburned species near the propellant surface react, and heat is transferred to the propellant surface. (b) Following a period of inert heating and continued pressurization, the surface temperature rises, and oxidizer and fuel species pyrolyze. (c) When the concentration of oxidizer and fuel species and the local gas-phase temperature are sufficiently high, intense gas-phase reactions begin.

5. The augmentation in heat feedback to the propellant at higher pressurization is a result of a combination of the following mechanisms: heating due to compression wave reflection at the closed end; heat release due to burning of unreacted igniter species near the tip, behind the reflected compression wave; and enhanced heat transfer due to recirculating hot gas near the tip.

6. Solutions revealed significant temperature non-uniformity implying two-dimensional effects which must be included in modeling composite propellant ignition.

7. More accurate chemical kinetic constants pertaining to ignition are needed to describe the pyrolysis and gas-phase reactions for more precise prediction of ignition delay times.

Important conclusions that can be drawn from the crack propagation investigation are described below. Even though the study presented in this report is only a first step in the investigation of crack propagation in a burning solid propellant, several interesting facts about the phenomenon have been observed and are summarized below:

1. Crack propagation velocities of 20 to 70 m/s were measured in a burning composite solid propellant. These velocities are in the same range as those reported in non-burning dynamic testing of inert propellants and rubbers.

2. It was found that cracks propagated at a constant velocity when subjected to a constant rate of internal pressurization.

3. It was observed that there is a characteristic difference in crack propagation processes between low and high rates of pressurization. The crack tip geometry maintained its original contour for low dp/dt. However, a fan region above the crack tip (accompanied by a squaring off of the tip region) was observed for high pressurization rates in the order of 20,000

MPa/s. The uneven multiple front of the crack tip and the appearance of the fan region suggests the occurrence of crack branching and micro-structure damage.

4. A tentative experimental correlation showed a stronger dependence of crack propagation velocity on pressurization rate than predictions based solely on the elastic-glassy transition behavior of viscoelastic material during dynamic loading. The reason for this discrepancy is unknown, and further research in the propagation of burning solid propellant cracks is needed.

REFERENCES

1. Kumar, M., Kuo, K. K., Kulkarni, A. K., and Wills, J. E., "Ignition of Composite Propellants under Rapid Pressure Loading," Annual Report to Office of Naval Research, Arlington, Va., Sept. 1981.

2. Lengelle, G., Brulard, J., and Montet, H., "Combustion Mechanisms of Composite Solid Propellants," Sixteenth Symposium (International) on Combustion, 1976, pp. 1257-1269.

3. Kishore, K. and Jois, G. V., "Chemistry of Ignition and Combustion of Ammonium Perchlorate Based Propellants," Fundamentals of Combustion of Solid Propellants, Edited by K. K. Kuo and M. Summerfield, AIAA Progress Series in Astronautics and Aeronautics, to be published.

4. Guirao, C. and Williams, F. A., "A Model for Ammonium Perchlorate Deflagration Between 20 and 100 atm," AIAA Journal, Vol. 9, July 1971, pp. 1345-1356.

5. Beckstead, M. W., Derr, R. L., and Price, C. F., "A Model for Composite Solid-Propellant Combustion Based on Multiple Flames," AIAA Journal, Vol. 8, Dec. 1970, pp. 2200-2207.

6. Pearson, G. S., "Perchlorate Oxidizers," Oxidation and Combustions Reviews, Vol. 4, 1969, pp. 1-92.

7. Jacobs, P. W. M. and Whitehead, H. M., "Decomposition and Combustion of Ammonium Perchlorate," Chemical Reviews, Vol. 69, Aug. 1969, pp. 551-590.

8. Rosser, W. A., Jr., Inami, S. H., and Wise, H., "Thermal Diffusivity of Ammonium Perchlorate," AIAA Journal, Vol. 4, April 1966, pp. 663-666.

9. Varney, A. M. and Strahle, W. C., "Thermal Decomposition Studies of Some Solid Propellant Binders," Combustion and Flame, Vol. 16, 1971, pp. 1-7.

10. Gordon, S. and McBride, B. J., "Computer Program for Calculation of Complex Chemical Equilibrium Compositions, Rocket Performance, Incident and Reflected Shocks, and Chapman-Jougnet Detonations," NASA SP-273, 1971.

11. Price, E. W., Panyam, R. A., Sigman, R. K., and Sambamurthy, J. K., "Solid Propellant Combustion Zone Microstructure," AIAA Paper 82-1113, AIAA/SAE/ASME 18th Joint Propulsion Conference, Cleveland, Ohio, June 1982.

12. Kumar, M., Wills, J. E., Kulkarni, A. K., and Kuo, K. K., "Ignition of Composite Propellants in a Stagnation Region under Rapid Pressure Loading," Nineteenth International Symposium on Combustion, Haifa, Israel, Aug. 1982.

13. Kulkarni, A. K., Kumar, M., and Kuo, K. K., "A Comprehensive Ignition Model for Composite Solid Propellants," Eighteenth JANNAF Combustion Meeting, Pasadena, California, CPIA Publication 347, Vol. III, October 1981, pp. 215-224.

14. Wills, J. E., Kumar, M., Kulkarni, A. K., Hund, M., and Kuo, K. K., "Investigation of Composite Propellant Ignition Under Rapid Pressurization," Eighteenth JANNAF Combustion Meeting, Pasadena, California, CPIA Publication 347, Vol. III, October 1981, pp. 243-262.

15. Wills, J. E., Kumar, M., Kulkarni, A. K., and Kuo, K. K., "Abrupt Ignition of AP-Based Composite Propellant Under Severe Gas Loading Conditions," 1982 JANNAF Propulsion Systems Hazards Meeting, China Lake, California, April 1982.

16. Kumar, M., Wills, J. E., Kulkarni, A. K., and Kuo, K. K., "A Model for AP-Based Composite Propellant Ignition, Including Gas-Phase and Subsurface Reactions," AIAA Paper No. 82-1109, AIAA/ASME/SAE Joint Propulsion Conference, Cleveland, Ohio, June 1982.

17. Siefert, J. G., Kumar, M., and Kuo, K. K., "Experimental Observations of Crack Propagation in Burning Solid Propellants," Nineteenth JANNAF Combustion Meeting, Greenbelt, Maryland, October 1982.

18. Kumar, M. and Kuo, K. K., "Effect of Deformation on Flame Spreading and Combustion in Propellant Cracks," AIAA Journal, Vol. 19, Dec. 1981, pp. 1580-1589.

19. Kulkarni, A. K., Kumar, M. and Kuo, K. K., "A Review of Solid Propellant Ignition Studies," AIAA Journal, Vol. 20, Feb. 1982, p. 243.

20. Knauss, W. G., "On the Steady Propagation of a Crack in a Viscoelastic Sheet: Experiments and Analysis," in Deformation and Fracture of High Polymers, eds. H. H. Kausch et al., 501-540, Plenum Press, 1973.

21. Knauss, W. G., "Fracture of Solids Possessing Deformation Rate Sensitive Material Properties," AMD-Vol. 19, The Mechanics of Fracture, ASME, 1976.

22. Schapery, R. A., "A Theory of Crack Initiative and Growth in Viscoelastic Media I, II, and III," Intl. J. Fracture, 11, 141-159, 369-388, and 549-562, 1975.

23. Francis, E. C., Carlton, C. H., and Thompson, R. E., "Viscoelastic Rocket Grain Fracture Analysis," Intl. J. Fracture, 10, 1974.

24. Langlois, G. and Gonard, R., "A New Law for Crack Propagation in a Solid Propellant," AIAA/SAE 14th Joint Propulsion Conference, AIAA Paper No. 78-1099, Las Vegas, NV, July 25-27, 1978.

25. Kim, K. S. and Knauss, W. G., "Dynamic Fracture in Visoelastic Solids," Annual Report to ONR, July 2, 1981.

26. Swanson, S. R., "Crack Velocity Measurements in Solithane 113," Annual Report to ONR, January 12, 1982.

27. Gent, A. N. and Marteny, P., "Crack Velocities in Natural Rubber," Technical Report No. 7 to ONR, May 1982.

28. Swanson, S. R., "An Experimental Study of Dynamic Crack Propagation in a Filled Rubber," 16th Ann. Meeting Soc. Eng. Sci., Northwestern University, September 5-7, 1979.

29. Fitzgerald, J. E., Handbook for the Engineering Structural Analysis of Solid Propellants, University of Utah, 1971.

APPENDIX A

Details of the Numerical Scheme

The coordinate transformation described by Eq. (37) and Eq. (38) is used to map the (r, z) coordinates in the physical space to (r, s) coordinate in the transformed space. The transformed governing equations for the solid and gas phases take the following form.

(A) Solid Phase Equations:

Oxidizer:

$$\rho_{ox,s} C_{ox,s} \frac{\partial T}{\partial t} = K_{ox,s} [A_s^2 (1+s)^2 \frac{\partial^2 T}{\partial s^2} + A_s^2 (1+s) \frac{\partial T}{\partial s}]$$

$$+ K_{ox,s} [\frac{1}{r} \frac{\partial T}{\partial r} + \frac{\partial^2 T}{\partial r^2}] + \dot{q}''_{ox,s} \qquad (A-1)$$

Fuel:

$$\rho_{F,s} C_{F,s} \frac{\partial T}{\partial t} = K_{F,s} [A_s^2 (1+s)^2 \frac{\partial^2 T}{\partial s^2} + A_s^2 (1+s) \frac{\partial T}{\partial s}]$$

$$+ k_{F,s} [\frac{1}{r} \frac{\partial T}{\partial r} + \frac{\partial^2 T}{\partial r^2}] + \dot{q}''_{F,s} \qquad (A-2)$$

(B) Gas Phase Equations:

Continuity:

$$\frac{\partial \rho_g}{\partial t} + A_g (1-s) \frac{\partial (\rho g V_Z)}{\partial s} = 0 \qquad (A-3)$$

Energy:

$$C_p \rho_g \frac{\partial T}{\partial t} + [\rho_g c_p V_{Z\ g} (1-s) + K_g A_g^2 (1-s)] \frac{\partial T}{\partial s} - \frac{\partial P}{\partial t}$$

$$= K_g A_g^2 (1-s)^2 \frac{\partial^2 T}{\partial s^2} + Kg (\frac{1}{r} \frac{\partial T}{\partial r} + \frac{\partial^2 T}{\partial r^2}) + \dot{q}'''_g \qquad (A-4)$$

Species

$$\rho_g \frac{\partial Y_i}{\partial t} + \rho_g V_Z A_g (1-s) \frac{\partial Y_i}{\partial s} = \frac{1}{r} \frac{\partial}{\partial r} (r D \rho_g \frac{\partial Y_i}{\partial r}) + \dot{\omega}'''_i \qquad (A-5)$$

where $i = 1$, 2, 3, and 4 represent oxidizer, NH_3, $HClO_4$, and fuel, respectively.

A second transformation is used to map the (r, s) coordinates into (r, s'). This transformation is described by the following equation.

$$s' = -s \text{ for } -1 \leq s < 0$$
$$s' = s \text{ for } 0 \leq s \leq 1 \tag{A-6}$$

This transformation affects only the solid phase equations and these equations take the following form.

Oxidizer:
$$\rho_{ox,s} \, C_{ox,s} \frac{\partial T}{\partial t} = K_{ox,s} [A_s^2(1-s')^2 \frac{\partial^2 T}{\partial s'^2} - A_s^2(1-s') \frac{\partial T}{\partial s'}]$$
$$+ K_{Ox,s} [\frac{1}{r} \frac{\partial T}{\partial r} + \frac{\partial^2 T}{\partial r^2}] + \dot{q}''_{ox,s} \tag{A-7}$$

Fuel:
$$\rho_{F,s} C_{F,s} \frac{\partial T}{\partial t} = k_{F,c} [A_s^2(1-s') \frac{\partial^2 T}{\partial s'^2} - A_s^2(1-s') \frac{\partial T}{\partial s'}]$$
$$+ k_{ox,s} [\frac{1}{r} \frac{\partial T}{\partial r} + \frac{\partial^2 T}{\partial r^2}] + \dot{q}''_{F,s} \tag{A-8}$$

The gas phase equations are obtained by replacing s by s' and are mathematically identical to A-3, A-4 and A-5.

F.D. Approximations for Radial Derivatives Using Allen's Method

A three point, variable mesh, Allen's Method, is used to approximate derivatives in the radial direction. Allen's Method is chosen in preference to Central Difference Method because it offers a better approximation of the derivative near the axis of the computational domain. Figure A-1 shows a z = constant plane near the axis showing nodes with different radii.

The following paragraphs describe the derivation of the difference formula using Allen's Method. The radial derivative term appears in the following form in our governing equations.

$$\frac{\partial^2 \eta}{\partial r^2} + \frac{1}{r}\frac{\partial \eta}{\partial r} \quad \text{(where } \eta \text{ could be temperature or species mass fraction)}$$

We define the following quantities:

$$\Omega \equiv \frac{\partial^2 \eta}{\partial r^2} + \frac{1}{r}\frac{\partial \eta}{\partial r} \tag{A-9}$$

Ω is assumed to be locally constant

$$\Gamma \equiv \frac{\partial \eta}{\partial r} \tag{A-10}$$

Thus $\dfrac{d\Gamma}{dr} + \dfrac{1}{r}\Gamma = \Omega$ $\qquad$ (A-11)

The solution for Eq. (A-11) is

$$\Gamma = \frac{1}{r}\int \Omega\, r\, dr + \frac{c}{r} = \frac{\Omega}{2}r + \frac{A}{r} \tag{A-12}$$

$$\therefore \ \eta = \int \Gamma dr = \frac{\Omega}{4}r^2 + A\ \ell n r + B \tag{A-13}$$

To evaluate the constants Ω, A, B in Eq.(A-13), we write η at three consecutive points $j-1$, j, $j+1$.

$$\eta_{j-1} = \frac{\Omega}{4}r_{j-1}^2 + A\ \ell n r_{j-1} + B \tag{A-14}$$

$$\eta_{j} = \frac{\Omega}{4}r_{j}^2 + A\ \ell n r_{j} + B \tag{A-15}$$

$$\eta_{j+1} = \frac{\Omega}{4}r_{j+1}^2 + A\ \ell n r_{j+1} + B \tag{A-16}$$

We solve Eqs. (A-14), (A-15), and (A-16) to get the following value for Ω.

$$\Omega = \frac{4\ \ell n\,(r_{j+1}/r_j)}{Q}\,(\eta_{j-1}-\eta_j) + \frac{4\ \ell n\,(r_j/r_{j-1})}{Q}\,(\eta_{j+1}-\eta_j) \tag{A-17}$$

where $Q = \ell n\,(r_{j+1}/r_j)(r_{j-1}^2-r_j^2) + \ell n\,(r_j/r_{j-1})(r_{j+1}^2-r_j^2)$ $\qquad$ (A-18)

Treatment of Nodes on the Axis and One Node Away from the Axis

(a) Approximation of Radial Derivative Term on the Axis:

Assume that the scalar variable η is symmetric about the axis; thus,

$$\frac{\partial \eta}{\partial r} \Big)_{r=0} = 0 \qquad \text{(A-19)}$$

Use the Taylor's series to expand the term $\frac{\partial \eta}{\partial r}$ about $r=0$

$$\frac{\partial \eta}{\partial r} = \frac{\partial \eta}{\partial r}\Big)_{r=0}^{0} + r \frac{\partial^2 \eta}{\partial r^2}\Big)_{r=0} + \frac{r}{2} \frac{\partial^2 \eta}{\partial r^3}\Big)_{r=0} + \cdots \qquad \text{(A-20)}$$

We neglect the terms with order higher than 2, and divide Eq. (A-20) by r

$$\frac{1}{r} \frac{\partial \eta}{\partial r} \simeq \frac{\partial^2 \eta}{\partial r^2}\Big)_{r=0} \qquad \text{(A-21)}$$

Thus for the nodes on the axis

$$\frac{1}{r} \frac{\partial \eta}{\partial r} + \frac{\partial^2 \eta}{\partial r^2} = 2 \frac{\partial^2 \eta}{\partial r^2} \qquad \text{(A-22)}$$

We define $\dfrac{\partial^2 \eta}{\partial r^2} = \Omega'$ \qquad \text{(A-23)}

$\therefore$ From Eqs. (A-22) and (A-23)

$$\frac{\partial \eta}{\partial r} = \Omega' r$$

$$\eta = \frac{\Omega'}{2} r^2 + B'$$

$$\therefore \eta = \frac{\Omega'}{2} r^2 + B' \qquad \text{(A-24)}$$

at $r = 0 = r_1$

$$\eta_1 = B'$$

$$\eta_2 = \frac{\Omega'}{2} r_2^2 + \eta_1$$

Thus, $\Omega' = \dfrac{2(\eta_2 - \eta_1)}{r_2^2}$ \qquad \text{(A-25)}

From Eqs. (A-22), (A-23), and (A-25), we have

$$\frac{1}{r} \frac{\partial \eta}{\partial r} + \frac{\partial^2 \eta}{\partial r^2} = 2 \frac{\partial^2 \eta}{r^2} = \frac{4(\eta_2 - \eta_1)}{r_2^2} \qquad \text{(A-26)}$$

for nodes on the axis.

(b) Approximation of the Radial Derivative Term One Node Away from the Axis

Consider the most general expression for η given by Eq. (A-13). As we approach the axis, we have

$$\eta = \lim_{r \to o} (\frac{\Omega}{4} r^2 + A \ln r + B)$$
$$= -\infty A + B$$

This result is unreasonable, hence we conclude that $A = 0$ near the axis.

Thus, very near the axis we have

$$\eta = \frac{\Omega}{4} r^2 + B \tag{A-27}$$

We use Eq. (A-27) for node 2 and 3

$$\eta_2 = \frac{\Omega}{4} r_2^2 + B \tag{A-28}$$

$$\eta_3 = \frac{\Omega}{4} r_3^2 + B \tag{A-29}$$

Solving Eqs. (A-28) and (A-29) simultaneously we get

$$\Omega = \frac{4(\eta_3 - \eta_2)}{r_3^2 - r_2^2} \tag{A-30}$$

Substituting this expression in Eq. (A-9), we get for node 2

$$\frac{\partial^2 \eta}{\partial r^2} + \frac{1}{r} \frac{\partial \eta}{\partial r} = \frac{4(\eta_3 - \eta_2)}{r_3^2 - r_2^2} \tag{A-31}$$

Solution of the F.D. Equations

A generalized Crank Nicolson Algorithm was used to solve the finite difference equations obtained by the procedure described above. Figure A-2 represents the radial, axial and time coordinates for the above scheme. The algorithm developed had a facility to make the method either fully implicit or semi-implicit in time.

Following equations are obtained for the derivative terms in the governing equations. The parameter θ determines the implicitness of the method. A central difference scheme is used to approximate the axial derivatives, while Allen's method described in the previous section is used for the radial derivatives.

Temporal derivative:

$$\frac{\partial \eta}{\partial t} = \frac{\partial \eta}{\partial t}\bigg|_{i,j}^{k+\theta} = \frac{n_{i,j}^{k+1} - n_{i,j}^{k}}{\Delta t} \qquad \text{(A-32)}$$

Axial derivative:

$$\frac{\partial^2 \eta}{\partial s'^2} = \frac{\partial^2 \eta}{\partial s^2}\bigg|_{i,j}^{k+\theta} = \theta \frac{n_{i+1,j}^{k+1} - 2 n_{i,j}^{k+1} + n_{i-1,j}^{k+1}}{(\Delta s')^2} + (1-\theta) \frac{n_{i+1,j}^{k} - 2 n_{i,j}^{k} + n_{i-1,j}^{k}}{(\Delta s')^2}$$

$$\text{(A-33)}$$

Radial derivative:

$$\frac{1}{r}\frac{\partial \eta}{\partial r} + \frac{\partial^2 \eta}{\partial r^2} = \frac{1}{r}\frac{\partial r_i}{\partial r}\bigg|_{i,j}^{k+\theta} + \frac{\partial^2 \eta}{\partial r^2}\bigg|_{i,j}^{k+\theta} \qquad \text{(A-34)}$$

For internal nodes, the radial derivative can be expressed as

$$\frac{1}{r}\frac{\partial \eta}{\partial r} + \frac{\partial^2 \eta}{\partial r^2} = [\frac{4 \ln(r_{j+1}/r_j)}{Q} (n_{i,j-1}^{(k+1)} - n_{i,j}^{k+1}) + \frac{4 \ln(r_j/r_{j-1})}{Q} (n_{i,j+1}^{k+1} - n_{i,j}^{k+1})]$$

$$+ (1-\theta) [\frac{4 \ln(r_{j+1}/r_j)}{Q} (n_{i,j-1}^{k} - n_{i,j}^{k}) + \frac{4 \ln(r_j/r_{j-1})}{Q} (n_{i,j+1}^{k} - n_{i,j}^{k})]$$

$$\text{(A-35)}$$

where Q is defined by Eq. (A-18).

For nodes on the axis and one node away from the axis $(r = o = r_1$ and $r = r_2)$:

at $r = o = r_1$ (node on the axis)

$$\frac{1}{r}\frac{\partial \eta}{\partial r} + \frac{\partial^2 \eta}{\partial r^2} = \theta(\frac{4 n_{i,2}^{k+1} - 4 n_{i,1}^{k+1}}{r_2^2}) + (1-\theta) (\frac{4 n_{i,2}^{k} - 4 n_{i,1}^{k}}{r_2^2}) \qquad \text{(A-36)}$$

at $r = r_2$ (first node away from the axis)

$$\frac{1}{r}\frac{\partial \eta}{\partial r} + \frac{\partial^2 \eta}{\partial r^2} = \theta(\frac{4 n_{i,3}^{k+1} - 4 n_{i,2}^{k+1}}{r_3^2 - r_2^2}) + (1-\theta) (\frac{4 n_{i,3}^{k} - 4 n_{i,2}^{k}}{r_3^2 - r_2^2}) \qquad \text{(A-37)}$$

Quasilinearization of Source Terms

The source terms in energy equations and species equations are functions of temperature and species mass fraction. These quantities being the unknowns for which energy and species conservation equations are solved, quasilinearization of the source terms is required.

Let $F(T,Y_j)$ represent the general inhomogeneous term. By Taylor series expansion we write

$$F_{\ell+1}^{K+\theta} = F_{\ell}^{K+\theta} + (T_{\ell+1}^{K+\theta} - T_{\ell}^{K+\theta}) \frac{\partial F}{\partial T}\bigg|_{\ell}^{K+\theta} + (Y_{j,\ell+1}^{K+\theta} - Y_{j,\ell}^{K+\theta}) \frac{\partial F}{\partial Y_j}\bigg|_{\ell}^{K+\theta} \qquad (A-38)$$

The index $K+\theta$ represents a time step in the Crank-Nicolson algorithm, where for any variable U,

$$U^{K+\theta} = \theta U^{K+1} + (1-\theta)U^K \qquad (A-39)$$

The index ℓ represents the number of iterations of the quasilinearization loop, and j denotes different species.

The derivations $\frac{\partial F}{\partial T}$ and $\frac{\partial F}{\partial Y_j}$ are evaluated from the chemical reaction modelling described earlier.

The procedures described in this Appendix are incorporated in the program outlined in Fig. 3.
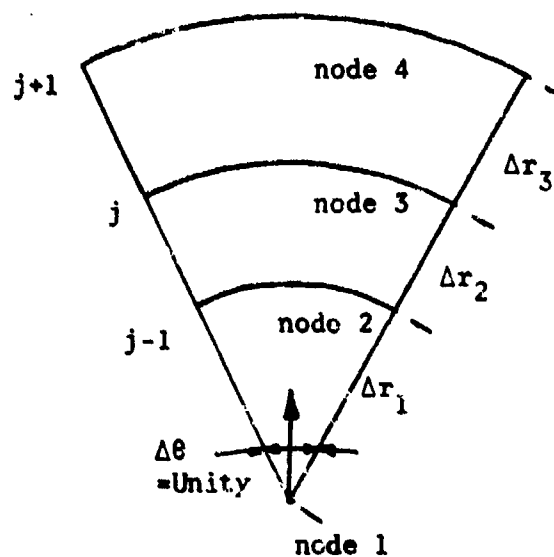
Fig. A-1 Two-Dimensional Finite Difference
Cylindrical Coordinate System Near
the Axis Showing a z=Constant Surface
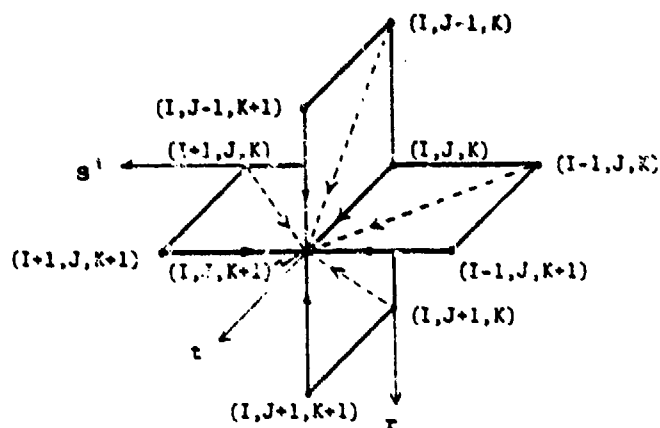
Fig. A-2 Generalized Crank-Nicolson Coordinates

DISTRIBUTION LIST

No. Copies

Dr. L.V. Schmidt   1
Assistant Secretary of the Navy
(R,E, and S) Room 5E 731
Pentagon
Washington, D.C.   20350

Dr. A.L. Slafkosky   1
Scientific Advisor
Commandant of the Marine Corps
Code RD-1
Washington, D.C.   20380

Dr. Richard S. Miller   10
Office of Naval Research
Code 413
Arlington, VA   22217

Mr. David Siegel   1
Office of Naval Research
Code 260
Arlington, VA   22217

Dr. R.J. Marcus   1
Office of Naval Research
Western Office
1030 East Green Street
Pasadena, CA   91106

Dr. Larry Peebles   1
Office of Naval Research
East Central   Regional Office
666 Summer Street, Bldg. 114-D
Boston, MA   02210

Dr. Phillip A. Miller   1
Office of Naval Research
San Francisco Area Office
One Hallidie Plaza, Suite 601
San Francisco, CA   94102

Mr. Otto K. Heiney   1
AFATL - DLDL
Elgin AFB, FL   32542

Mr. R. Geisler   1
ATTN: MKP/MS24
AFRPL
Edwards AFB, CA   93523

No. Copies

Dr. F. Roberto   1
Code AFRPL MKPA
Edwards AFB, CA   93523

Dr. L.H. Caveny   1
Air Force Office of Scientific
Research
Directorate of Aerospace Sciences
Bolling Air Force Base
Washington, D.C.   20332

Mr. Donald L. Ball   1
Air Force Office of Scientific
Research
Directorate of Chemical Sciences
Bolling Air Force Base
Washington, D.C.   20332

Dr. John S. Wilkes, Jr.   1
FJSRL/NC
USAF Academy, CO   80840

Dr. R.L. Lou   1
Aerojet Strategic Propulsion Co.
P.O. Box 15699C
Sacramento, CA   95813

Dr. V.J. Keenan   1
Anal-Syn Lab Inc.
P.O. Box 547
Paoli, PA 19301

Dr. Philip Howe   1
Army Ballistic Research Labs
ARRADCOM
Code DRDAR-BLT
Aberdeen Proving Ground, MD 21005

Mr. L.A. Watermeier   1
Army Ballistic Research Labs
ARRADCOM
Code DRDAR-BLI
Aberdeen Proving Ground, MD   21005

Dr. W.W. Wharton   1
Attn: DRSMI-RKL
Commander
U.S. Army Missile Command
Redstone Arsenal, AL   35898

DISTRIBUTION LIST

No. Copies		No. Copies

Dr. R.G. Rhoades   1
Commander
Army Missile Command
DRSMI-R
Redstone Arsenal, AL 35898

Dr. E.H. Debutts   1
Hercules Inc.
Baccus Works
P.O. Box 98
Magna, UT 84044

Dr. W.D. Stephens   1
Atlantic Research Corp.
Pine Ridge Plant
7511 Wellington Rd.
Gainesville, VA 22065

Dr. James H. Thacher   1
Hercules Inc. Magna
Baccus Works
P.O. Box 98
Magna, UT 84044

Dr. A.W. Barrows   1
Ballistic Research Laboratory
USA ARRADCOM
DRDAR-BLP
Aberdeen Proving Ground, MD 21005

Mr. Theordore M. Gilliland   1
Johns Hopkins University APL
Chemical Propulsion Info. Agency
Johns Hopkins Road
Laurel, MD 20810

Dr. C.M. Frey   1
Chemical Systems Division
P.O. Box 358
Sunnyvale, CA 94086

Dr. R. McGuire   1
Lawrence Livermore Laboratory
University of California
Code L-324
Livermore, CA 94550

Professor F. Rodriguez   1
Cornell University
School of Chemical Engineering
Olin Hall, Ithaca, N.Y. 14853

Dr. Jack Linsk   1
Lockheed Missiles & Space Co.
P.O. Box 504
Code Org. 83-10, Bldg. 154
Sunnyvale, CA 94088

Defense Technical Information   12
Center
DTIC-DDA-2
Cameron Station
Alexandria, VA 22314

Dr. B.G. Craig   1
Los Alamos National Lab
P.O. Box 1663
NSP/DOD, MS-245
Los Alamos, NM 87545

Dr. Rocco C. Musso   1
Hercules Aerospace Division
Hercules Incorporated
Alleghany Ballistic Lab
P.O. Box 210
Washington, D.C. 21502

Dr. R.L. Rabie   1
WX-2, MS-952
Los Alamos National Lab.
P.O. Box 1663
Los Alamos NM 37545

Dr. Ronald L. Simmons   1
Hercules Inc. Eglin
AFATL/DLDL
Eglin AFB, FL 32542

Dr. R. Rogers, WX-2   1
Los Alamos Scientific Lab.
P.O. Box 1663
Los Alamos, NM 87545

DISTRIBUTION LIST

	No. Copies		No. Copies
Mr. R. Brown Naval Air Systems Command Code 330 Washington, D.C. 20361	1	Dr. J. Schnur Naval Research Lab. Code 6510 Washington, D.C. 20375	1
Dr. H. Rosenwasser Naval Air Systems Command AIR-310C Washington, D.C. 20360	1	Mr. R. Beauregard Naval Sea Systems Command SEA 64E Washington, D.C. 20362	1
Mr. B. Sobers Naval Air Systems Command Code 03P25 Washington, D.C. 20360	1	Mr. G. Edwards Naval Sea Systems Command Code 62R3 Washington, D.C. 20362	1
Dr. L.R. Rothstein Assistant Director Naval Explosives Dev. Engineering Dept. Naval Weapons Station Yorktown, VA 23691	1	Mr. John Boyle Materials Branch Naval Ship Engineering Center Philadelphia, PA 19112	1
Dr. Lionel Dickinson Naval Explosive Ordnance Disposal Tech. Center Code D Indian Head, MD 20640	1	Dr. H.G. Adolph Naval Surface Weapons Center Code R11 White Oak Silver Spring, MD 20910	1
Mr. C.L. Adams Naval Ordnance Station Code PM4 Indian Head, MD 20640	1	Dr. T.D. Austin Naval Surface Weapons Center Code R16 Indian Head, MD 20640	1
Mr. S. Mitchell Naval Ordnance Station Code 5253 Indian Head, MD 20640	1	Dr. T. Hall Code R-11 Naval Surface Weapons Center White Oak Laboratory Silver Spring, MD 20910	1
Dr. William Tolles Dean of Research Naval Postgraduate School Monterey, CA 93940	1	Mr. G.L. Mackenzie Naval Surface Weapons Center Code R101 Indian Head, MD 20640	1
Naval Research Lab. Code 6100 Washington, D.C. 20375	1	Dr. K.F. Mueller Naval Surface Weapons Center Code R11 White Oak	1

DISTRIBUTION LIST

No. Copies		No. Copies	
Mr. J. Murrin Naval Sea Systems Command Code 62R2 Washington, D.C. 20362	1	Dr. A. Nielsen Naval Weapons Center Code 385 China Lake, CA 93555	1
Dr. D.J. Pastine Naval Surface Weapons Cneter Code RO4 White Oak Silver Spring, MD 20910	1	Dr. R. Reed, Jr. Naval Weapons Center Code 388 China Lake, CA 93555	1
Mr. L. Roslund Naval Surface Weapons Center Code R122 White Oak, Silver Spring MD 20910	1	Dr. L. Smith Naval Weapons Center Code 3205 China Lake, CA 93555	1
Mr. M. Stosz Naval Surface Weapons Center Code R121 White Oak Silver Spring, MD 20910	1	Dr. B. Douda Naval Weapons Support Center Code 5042 Crane, Indiana 47522	1
Dr. E. Zimmet Naval Surface Weapons Center Code R13 White Oak Silver Spring, MD 20910	1	Dr. A. Faulstich Chief of Naval Technology MAT Code 0716 Washington, D.C. 20360	1
Dr. D. R. Derr Naval Weapons Center Code 388 China Lake, CA 93555	1	LCDR J. Walker Chief of Naval Material Office of Naval Technology MAT, Code 0712 Washington, D.C. 20360	1
Mr. Lee N. Gilbert Naval Weapons Center Code 3205 China Lake, CA 93555	1	Mr. Joe McCartney Naval Ocean Systems Center San Diego, CA 92152	1
Dr. E. Martin Naval Weapons Center Code 3858 China Lake, CA 93555	1	Dr. S. Yamamoto Marine Sciences Division Naval Ocean Systems Center San Diego, CA 91232	1
Mr. R. McCarten Naval Weapons Center	1	Dr. G. Bosmajian Applied Chemistry Division Naval Ship Research & Development Center Annapolis, MD 21401	1

6/81

DISTRIBUTION LIST

No. Copies		No. Copies

Dr. J.F. Kincaid 1
Strategic Systems Project
Office
Department of the Navy
Room 901
Washington, D.C. 20376

Strategic Systems Project Office 1
Propulsion Unit
Code SP2731
Department of the Navy
Wahsington, D.C. 20376

Mr. E. L. Throckmorton 1
Strategic Systems Project Office
Department of the Navy
Room 1048
Washington, D.C. 20376

Dr. D.A. Flanigan 1
Thiokol
Huntsville Division
Huntsville, Alabama 35807

Mr. G.F. Mangum 1
Thiokol Corporation
Huntsville Division
Huntsville, Alabama 35807

Mr. E.S. Sutton 1
Thiokol Corporation
Elkton Division
P.O. Box 241
Elkton, MD 21921

Dr. G. Thompson 1
Thiokol
Wasatch Division
MS 240 P.O. Box 524
Brigham City, UT 84302

Dr. T.F. Davidson 1
Technical Director
Thiokol Corporation
Government Systems Group
P.O. Box 9258
Odgen, Utah 84409

Dr. C.W. Vriesen 1
Thiokol Elkton Division
P.O. Box 241
Elkton, MD 21921

Dr. J.C. Hinshaw 1
Thiokol Wasatch Division
P.O. Box 524
Brigham City, Utah 83402

U.S. Army Research Office 1
Chemical & Biological Sciences
Division
P.O. Box 12211
Research Triangle Park
NC 27709

Dr. R.F. Walker 1
USA ARRADCOM
DRDAR-LCE
Dover, NJ 07801

Dr. T. Sinden 1
Munitions Directorate
Propellants and Explosives
Defence Equipment Scarf
British Embassy
3100 Massachusetts Ave.
Washington, D.C. 20008

LTC B. Loving 1
AFROL/LK
Edwards AFB, CA 93523

Professor Alan N. Gent 1
Institute of Polymer Science
University of Akron
Akron, OH 44325

Mr. J.M. Frankle 1
Army Ballistic Research Labs
ARRADCOM
Code DRDAR-BLI
Aberdeen Proving Ground, MD 21005

DYN   6/81

DISTRIBUTION LIST

<u>No. Copies</u>   <u>No. Copies</u>

Dr. Ingo W. May   1   Dr. J. P. Marshall   1
Army Ballistic Research Labs   Dept. 52-35, Bldg. 204/2
ARRADCOM   Lockheed Missile & Space Co.
Code DRDAR-BLI   3251 Hanover Street
Aberdeen Proving Ground, MD 21005   Palo Alto, CA 94304

Professor N.W. Tschoegl   1   Ms. Joan L. Janney   1
California Institute of Tech   Los Alamos National Lab
Dept. of Chemical Engineering   Mail Stop 920
Pasadena, CA 91125   Los Alamos, NM 87545

Professor M.D. Nicol   1   Dr. J. M. Walsh   1
University of California   Los Alamos Scientific Lab
Dept. of Chemistry   Los Alamos, NM 87545
405 Hilgard Avenue
Los Angeles, CA 90024   Professor R. W. Armstrong   1
                                             Univ. of Maryland
Professor A. G. Evans   1   Department of Mechanical Eng.
University of California   College Park, MD 20742
Berkeley, CA 94720
                                             Prof. Richard A. Reinhardt 1
Professor T. Litovitz   1   Naval Postgraduate School
Catholic Univ. of America   Physics & Chemistry Dept.
Physics Department   Monterey, CA 93940
520 Michigan Ave., N.E.
Washington, D.C. 20017   Dr. R. Bernecker   1
                                             Naval Surface Weapons Center
Professor W. G. Knauss   1   Code R13
Graduate Aeronautical Lab   White Oak, Silver Spring, MD 20910
California Institute of Tech.
Pasadena, CA 91125   Dr. M. J. Kamlet   1
                                             Naval Surface Weapons Center
Professor Edward Price   1   Code R11
Georgia Institute of Tech.   White Oak, Silver Spring, MD 20910
School of Aerospace Engin.
Atlanta, Georgia 30332   Professor J. D. Achenbach   1
                                             Northwestern University
Dr. Kenneth O. Hartman   1   Dept. of Civil Engineering
Hercules Aerospace Division   Evanston, IL 60201
Hercules Incorporated
P.O. Box 210   Dr. N. L. Basdekas   1
Cumberland, MD 21502   Office of Naval Research
                                             Mechanics Program, Code 432
Dr. Thor L. Smith   1   Arlington, VA 22217
IBM Research Lab
D42.282   Professor Kenneth Kuo   1

DISTRIBUTION LIST

	No. Copies		No. Copies

Dr. S. Sheffield   1
Sandia Laboratories
Division 2513
P.O. Box 5800
Albuquerque, NM 87185

Dr. M. Farber   1
Space Sciences, Inc.
135 Maple Avenue
Monrovia, CA   91016

Dr. Y. M. Gupta   1
SRI International
333 Ravenswood AVenue
Menlo Park, CA 94025

Mr. M. Hill   1
SRI International
333 Ravenswood Avenue
Menlo Park, CA 94025

Professor Richard A. Schapery   1
Texas A&M Univ.
Dept of Civil Engineering
College Station, TX   77843

Dr. Stephen Swanson   1
Univ. of Utah
Dept. of Mech. & Industrial
    Engineering
MEB 3008
Salt Lake City, UT   84112

Mr. J. D. Byrd   1
Thiokol Corp. Huntsville
Huntsville Div.
Huntsville, AL   35807

Professor G. D. Duvall   1
Washington State University
Dept. of Physics
Pullman, WA 99163

Prof. T. Dickinson   1
Washington State University
Dept. of Physics
Pullman, WA 99163